



## Assessment of nanofibre dustiness by means of vibro-fluidization

Dirk Broßell <sup>\*</sup>, Elisabeth Heunisch, Asmus Meyer-Plath, Daphne Bäger, Volker Bachmann, Kerstin Kämpf, Nico Dziurawitz, Carmen Thim, Daniela Wenzlaff, John Schumann, Sabine Plitzko

Federal Institute for Occupational Safety and Health, Nöldnerstr. 40–42, D-10317 Berlin, Germany

### ARTICLE INFO

#### Article history:

Received 6 June 2018

Received in revised form 5 October 2018

Accepted 9 October 2018

Available online 11 October 2018

#### Keywords:

Vibro-fluidization

Dustiness testing

MWCNTs

Morphological particle characterization

WHO-fibre fraction

Risk assessment

### ABSTRACT

Dustiness testing probes for the propensity of a powdery material to release dust particles following agitation. For high aspect-ratio materials like nanotubes, the most important dust fraction is that of potentially carcinogenic fibres (WHO-fibres). We developed the fluidizer particularly for fibres that makes use of vibro-fluidization in order to effectively disentangle single fibres and agglomerates of multi-walled carbon nanotube powders. Counting rules for morphological characterization of collected particles by means of electron microscopy were established, allowing quantifying the WHO-fibre fraction. Dustiness tests on 15 different multi-walled carbon nanotubes were performed using two different levels of energy input for each material. The fluidizer accomplished bubbling fluidization for 13 out of the 15 multi-walled carbon nanotubes, resulting in continuous aerosol generation with stable particle number concentration and a high fraction of single fibres. Dustiness measurands like average particle number concentrations varied by three orders of magnitude. Morphological characterization of particles on aerosol samples proved to be essential to overcome the limitations of the applied aerosol instruments in quantifying the WHO-fibre fraction, therefore allowing material ranking based on associated risk. The materials showed strong ordering discrepancy when ranked based on total dustiness and WHO-fibre dustiness. Several multi-walled carbon nanotubes showed WHO-fibre concentrations high enough to potentially cause workplace exposure at hazardous concentration levels in case powders are handled carelessly.

© 2018 Published by Elsevier B.V.

### 1. Introduction

Carbon Nanotubes (CNT) have found widespread applications that underline their present industrial relevance for the development and manufacturing of innovative materials and products [1]. Their sustainability is challenged since several animal studies attributed a high carcinogenic potential to respirable multi-walled CNT (MWCNT) and other high aspect ratio materials (HAR materials, criterion: aspect ratio > 3:1) that are in accord with the fibre toxicological paradigm known for asbestos [2–7].

Strongest inhalative human exposure to particles and fibres is expected from aerosol generation processes, e.g. dust released by disintegrating the parent material [8]. The propensity of a material to produce dust following agitation, the so-called dustiness, depends on the agitation process as well as on material properties. Tests that are able to determine material dustiness under controlled conditions, thus enabling material comparison and ranking, are a powerful tool for risk assessment strategies like control banding [9]. Different measures for the dustiness and for the exposure potential of a process or material have been defined and discussed in the literature [10,11]. The most commonly used measures are dustiness indexes, the mass of released

dust per tested powder mass. In addition, dust is classified based on the mass median aerodynamic diameter into an inhalable, thoracic and respirable fraction. These measurands have been employed in the European standard EN 15051 for dustiness testing of granular bulk materials with particle release in the micrometre range [12] and also in the recently drafted prEN 17199 [13].

Dustiness indexes are by definition insensitive towards particle morphology and they have been employed mainly for particulates with mass-dependent toxicology, like granular biopersistent particles [14]. To reflect the morphology-driven toxicity of fibres, characterization of the dustiness of HAR materials requires new metrics since fibre toxicity is best described with the number of lung-deposited fibres. In case of inhalation exposure assessment to fibre-containing dust at the workplace, the respirable fibre concentration has to be determined number based [15]. This is aggravated by the facts that dust of HAR materials most often comprises also non-fibrous particles and fibres themselves have to be differentiated. By definition of the World Health Organization (WHO), fibres longer than 5 µm, thinner than 3 µm and with an aspect ratio larger than 3:1 (WHO-fibres, [16]) are considered respirable and potentially carcinogenic [4]. Aerosol characterization instruments employed in the abovementioned standards are unable to gather information on particle shape and morphology and thus to quantify the number of WHO-fibres in the released aerosol. In case HAR materials are tested for dustiness, prEN 17199 suggests aerosol sampling for

<sup>\*</sup> Corresponding author.

E-mail address: [brossell.dirk@baua.bund.de](mailto:brossell.dirk@baua.bund.de) (D. Broßell).

subsequent analysis with electron microscopy, if information on dust morphology is regarded to be important. However, morphological characterization is not standardized in form of counting rules for particles found on samples. The standard therefore only allows generating information about the total dustiness of a material while pointing out that fibres were present without actually quantifying the arguably most important and health-relevant dust fraction, namely WHO-fibres.

Three dustiness tests have been developed and standardized that agitate powders in order to aerosolize particles, which are the continuous drop method [17], the rotating drum [18] and vortex shaker [19,20]. They typically mimic specific handling or processing scenarios, like decantation of powders in case of the continuous drop. The first two have been part of EN 15051. Continuous drop and rotating drum have also been adapted in the prEN 17199 to the needs of powders containing nanoscale objects. This norm also describes standardized dustiness testing with a smaller version of the rotating drum and the vortex shaker. While applicability of the continuous drop and rotating drum methods to HAR materials has not been evaluated so far, the vortex shaker has been employed for CNTs [21–23]. With the vortex shaker, 14 CNTs of the NM-series of manufactured nanomaterials of the Joint Research Centre of the European Union (JRC) were tested for dustiness [24].

To compare dustiness tests, the kinetic energy of released particles has been used, which scales with the airflow velocity [11]. Such a description is incomplete since all dustiness tests transfer additional energy to de-agglomerate powder particles, which includes both breaking up cohesion between agglomerates and fragmentizing agglomerates, achieved by mechanical agitation. The energy input by agitation is difficult to quantify because the physics determining particle de-agglomeration is complex. For example, the vortex shaker agitates powder by means of a circular orbital motion of the sample test tube while airflow introduced from above aerosolizes particles. The energy input by wall-powder impacts is most likely non-uniform in the powder bed because of its irregularly shaped vessel, contributing to chaotic powder bed behaviour. As a result, applying vortex shaking requires great care in choosing multiple control parameters for reproducible results in dustiness testing [21].

In order to achieve well-controlled dustiness testing with HAR-materials, i.e. highly flexible aerosol generation with a large knowledge base, we studied the history of aerosol generation for animal inhalation studies. To provide nanotube aerosols for animal inhalation studies, continuous nanotube aerosol generation has been accomplished by electro-spraying stabilized MWCNT-suspensions [25]. More recently, dry dispersion of a binary mixture of MWCNT-powder and glass beads by means of a Venturi nozzle produced aerosols with a high fraction of individual fibres with stable particle number concentrations [26]. However, because both methods alter the test powder, they are not feasible for dustiness testing. Historically, vibro-fluidization has been applied to prepare aerosols from fibre containing asbestos powders, individualizing and aerosolizing entangled fibres effectively [27,28]. In the following, we will present our aerosol generator using vibro-fluidization for dustiness testing of powders containing HARM, short: fluidizer. It combines two different approaches to powder fluidization, bed vibration and gas fluidization of a vertically oriented powder column. This allows controlling their individual contributions to dust release, helps to regularize the powder movement and balance effects from wall-particle and from particle-particle impacts. A previous variant utilizing horizontal shaking was first described in a German publication [29]. The method can profit from a wealth of literature on gas and bed vibration fluidization also of nanoscale powders since the physics of such systems is of high importance for particle processing, e.g. [30–35].

In order to overcome the limitations by the applied aerosol instrumentation at determining health-relevant dustiness metrics for fibres, we developed a strategy for the morphological characterization of aerosol samples collected over the course of the dustiness test with the help of electron microscopy. It comprises counting rules based on morphological particle classes. Complementary to aerosol sampling for

subsequent electron microscopy, different aerosol monitors were connected to the fluidizer. With this instrumentation, not only the dustiness metrics demanded by prEN 17199 can be determined by applied aerosol instrumentation, but also health-relevant fibre fractions, in particular the WHO-fibre number fraction.

We aspired to perform dustiness tests with well-controlled and reproducible aerosol generation conditions. However, the conditions at which fluidized beds form depend on powder properties like particle size and tapped density [36] that were different for the MWCNT-powders we used. While changing the control parameters of the fluidizer, vibration intensity and sample flow rate, the powder beds were visually observed and the particle number concentration of the generated aerosol monitored. Conditions for which the majority of the powders showed equivalent vibro-fluidization behaviour were linked to characteristic time-dependencies of the particle number concentration. The establishment of equivalent concentration behaviours served as a quality criterion for comparability of dustiness tests. We then conducted a comparative study on the dustiness of 15 different MWCNT-powders. With the help of the morphological characterization, we assessed the exposure potential of MWCNTs in the context of the fibre toxicological paradigm and ranked them in the order of their propensity to release WHO-fibres.

## 2. Materials and methods

First, we quickly summarize the properties of the MWCNT materials. Subsequently, we give a description of how vibrational agitation of powders facilitated fluidization. Then, the section 'description of the experimental setup' describes the apparatus for aerosol generation and the test line for aerosol monitoring and sampling. We then formulate considerations of the energy input of the fluidizer. A short description of the standard operation procedure for performing dustiness tests employing the aerosol generator for fibres is given as well as counting rules for the morphological characterization by means of SEM. The list of measurands used in this study was taken from the drafted standard prEN 17199 and adapted to the requirements of fibres.

### 2.1. Materials

In this study, 15 different MWCNT materials were tested with the fluidizer. The relevant material properties, as stated by the manufacturers or measured in our laboratory, are summarized in Table 1. The materials were purchased in the years 2011–2016. All materials were synthesized in a chemical vapour deposition (CVD) process. Some of the powders were industrial grade, others of high purity. Charge/LOT-numbers and BET surface areas were not known in some cases.

Material samples were obtained by pouring powder on 12-mm carbon cohesive tabs (Plano G3347). Fig. 1 shows six SEM images of powder samples of (a, b) Baytubes C150P, (c, d) C2154 and (e, f) MWCNT-7. We show and describe those materials exemplarily, representing materials with small, medium and large outer tube diameters, respectively. Powders of materials with similar tube diameters also showed similar powder properties like tapped density. In the following, we name individually countable particles powder particles (at low magnification like 100×). Agglomerates are labelled as such when primary particles, in this case individual fibres, are visible. Naturally, powder particles were agglomerates.

Baytubes C150P in Fig. 1(a) showed particle sizes in the range of ca. 100–500 µm at a magnification of 100×, equivalent to values found in the literature [37,38]. The particles showed shard-like shape, i.e. with flat surface areas and edges. Fig. 1(b) shows a section of (a), marked by a white rectangle. It depicts a small spheroidal agglomerate adherent to a larger particle of Baytubes C150P at a 10,000× magnification. Such surface agglomerates were found on every powder particle with sizes ranging from ca. 1 µm to 50 µm. Agglomerates comprised a very large number of individual nanotubes tightly bundled up. This is reflected

**Table 1**  
Multi-walled carbon nanotube materials and their properties, tested with shaker. IG – Industrial Grade.

Material	Distributor	LOT	D* [nm]	L <sup>a</sup> [μm]	Purity <sup>a</sup>	BET <sup>a</sup> [m <sup>2</sup> /g]	ρ <sub>t</sub> <sup>b</sup> [g/cm <sup>3</sup> ]
ARIGM001	Arry Intl.	n/a	10–30	<15	IG (>80%)	>300	0.061
ARIGM002	Arry Intl.	n/a	30–70	5–15	IG (>80%)	>200	0.095
ARM006	Arry Intl.	n/a	20–30	<20 μm	>95 wt%	>200	0.206
Baytubes C150P	BTS	MIV-05-182	13	>1	>95%	n/a	0.197
C2148	TCI	5T2SB-ES	10	5–15	n/a	n/a	0.145
C2154	TCI	CCFL-JG	20–40	5–15	n/a	n/a	0.090
C2158	TCI	035NF-RT	60–100	>5	n/a	n/a	0.059
CNT-MW	Future Carbon	P0904291	10–25	1–10	95%	120	0.282
MRCSD	MER	n/a	140 ± 30	7 ± 2	>90%	n/a	0.085
MWCNT-7	Mitsui	061217-29	49.95 ± 0.63	5.29 ± 0.12	99.5%	22	0.013
NC 7000	Nanocyl	1167	9.5	1.5	IG (>90%)	250–300	0.054
NM 400	JRC	60048-60077	11 ± 3	0.85 ± 0.46	>99 wt%	254	0.052
NM 401	JRC	990025-990944	67 ± 24	4.05 ± 2.37	n/a	140	0.012
NTX3	Nanothinx	n/a	25–40	>10	> 91%	200–250	0.070
SMW 100	SWeNT	MKBD4153V	6–9	5	>98%	n/a	0.101

<sup>a</sup> As stated by the manufacturer

<sup>b</sup> Determined by measuring powder bed volume at applied powder mass of 300 mg

by the relatively large tapped density of ca.  $\rho_t = 0.2$  g/cm<sup>3</sup>. Agglomerates also appeared to comprise non-fibrous particles, maybe leftover catalyst nanoparticles stemming from synthesis. In addition, even fibre-shaped bundles of MWCNTs protruding the particle surface were found on some powder particles.

The particle size range of C2154, shown in Fig. 1(c) at a magnification of 100×, was much wider, comprising particles with sizes ranging from ca. 10 μm to 500 μm, appearing spheroidal but exhibiting many surface pores. The smaller particles in the size range of 10 μm to 50 μm were much more numerous and they stuck to the surface of the

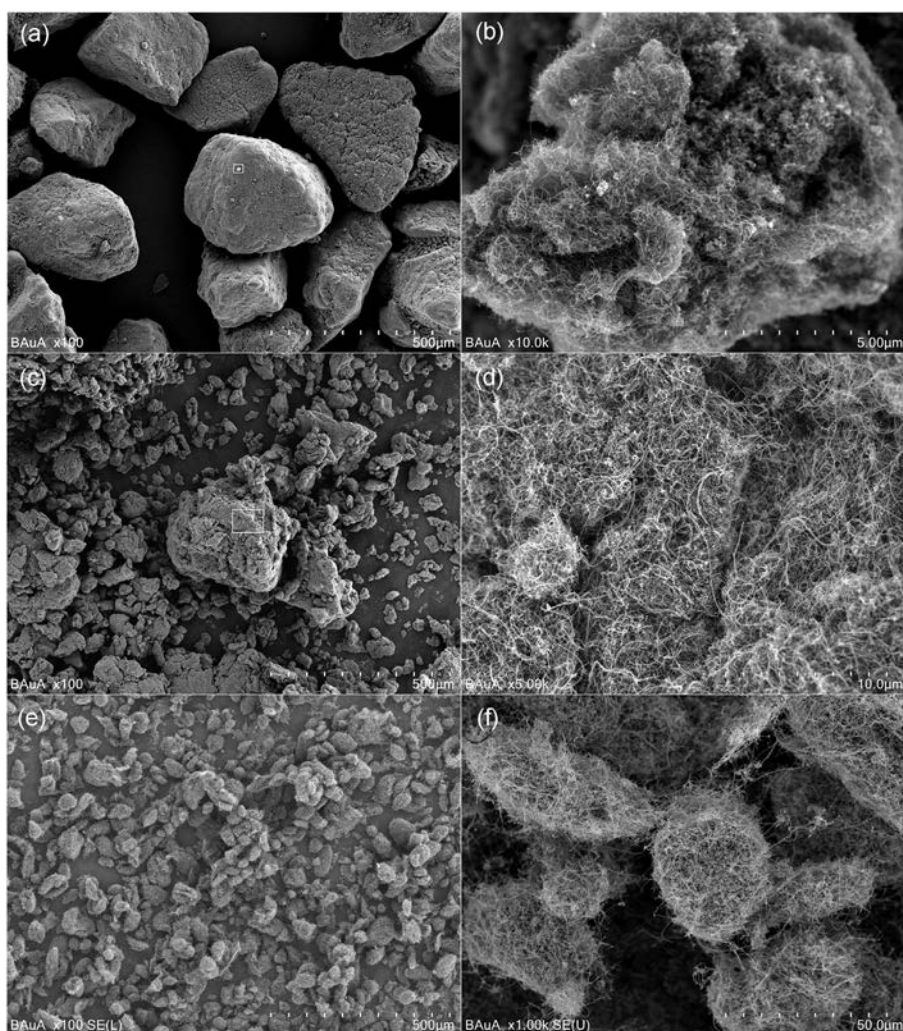


**Fig. 1.** SEM images of base material samples of Baytubes C150P (a, b), C2154 (c, d) and MWCNT-7 (e, f). The left images show the respective powder particles in with 100× magnification. The right images show the surface of the particles in larger magnification of 10,000× (b), 5000× (d) and 1000× (f). For (b) and (d), the image acquisition locations are marked on (a) and (c) with white rectangles, respectively.

larger particles. The section marked by a white rectangle is shown in Fig. 1(d) with 5000× magnification. The image shows an agglomerate with ca. 5 µm diameter bound to the particle surface by entanglement of protruding nanotubes. Individual nanotubes appeared to occupy less space compared to Baytubes C150P, reflected in a smaller tapped density of  $\rho_t = 0.09 \text{ g/cm}^3$ .

The powder of MWCNT-7, shown in Fig. 1(e) at a magnification of 100×, exhibited particle sizes in the range of 5–50 µm. A clear distinction between particles and agglomerates could not be made, demonstrated by Fig. 1(f) showing an image with a magnification of 1000×, at which not only whole particles are visible but also individual nanotubes. Entanglement of protruding fibres caused agglomerates to be strung together over vast sections of the SEM images. Only a small volume fraction was occupied by MWCNTs, resulting in a small tapped density compared to other MWCNT materials of  $\rho_t = 0.013 \text{ g/cm}^3$ .

## 2.2. Aerosol generation by vibro-fluidization

Powder bed fluidization is a well-described phenomenon that is widely applied as a particle processing technology and we refer to methodological reviews for a detailed introduction [30,39,40]. In short, fluidization happens by an airflow traversing the powder column that is strong enough so that the hydrodynamic friction on the particles balances their weight. In a fluidized bed, particle dynamics are dominated by particle-particle and particle-gas interactions. Such interactions can be van-der-Waals force, Coulomb force or liquid bridging that bind particles to the fluidized bed or local shear forces by the medium that can liberate and transport particles.

In case of low airflow velocities that are not sufficient for fluidization, air moves through voids in the powder bed, called packed bed. Fluidization happens at the so-called minimum fluidization velocity at which the powder bed expands its volume, visible by an increase of bed height. A so-called stationary fluidized bed is described by a horizontal upper surface and homogenous density distribution throughout the powder bed that is lower than the tapped density of the packed bed. Stationary fluidized beds are difficult to establish in case particles are size distributed in the powder, as it is usually the case. Different particle sizes lead to non-uniform fluidization conditions. The wider a size distribution is the harder the establishment of a stationary fluidization becomes. For this reason, the flow rate used in practice is chosen higher than theoretically required for fluidization.

Gas that is not required for fluidization passes the fluidized bed in form of bubbles [41], forming where the gas is introduced, moving upwards and merging with other bubbles along the way. They carry some amount of particles inside as they drift upwards, called wake [42], filling roughly one third of the bubble volume. When a bubble emerges at the surface and bursts, its wake is ejected. Particles are picked up by the airstream in the process, in case the airflow velocity is sufficient so that the drag force overcomes gravity. Heavy particles drop down to the powder bed surface. Steady bubbling accompanied by continuous upwardly transport and ejection of powder material most likely causes continuous aerosol generation. The bubble size and so bubble flow rate is dependent on the rate of excess flow beyond what is required to establish the minimum fluidization velocity. Increasing the flow rate therefore causes more material to be transported upwards. Consequently, aerosol generation increases with flow rate. At high flow rates, bubbles might grow to a size that spans over powder bed, lifting the whole powder column upwards until it collapses. This state is called slugging bed. This is avoided when the powder bed height is smaller than its diameter. When increasing the flow rate even further, one observes formation and turbulent motion of agglutinations and bed voids until pneumatic transport sets in. The dynamics of such a turbulent bed are not well known [43].

In case cohesion between powder particles becomes too strong, gas bypassing by channelling through cracks forming along less dense spaces in the powder bed occurs and the bed remains packed. Fibre

entanglements contribute greatly to cohesion in powders of HARM. As shown in the previous section and in Fig. 1, entanglements occurring between agglomerates in powders are due to intertwining nanotubes that protrude the surfaces of their hosts and create hook-and-loop like mechanical interlocking. To liberate MWCNT-agglomerates and to fluidize the powder, this interlocking must be broken. This can be accomplished by external agitation of the powder bed that can be vibrational [44] and sound-assisted [45], amongst others. The fluidizer agitates the powder bed by vertical vibration of the powder column. Literature about vibro-fluidization uses the dimensionless vibration intensity  $\Gamma$  to scale the shaking strength. It is defined as the ratio of the vibrational  $a = A(2\pi f)^2$  and gravitational acceleration  $g = 9.81 \text{ m/s}^2$ , where  $A$  is the amplitude and  $f$  the frequency of the oscillation:

$$\Gamma = \frac{a}{g}. \quad (1)$$

Without airflow, the vibrational must overcome the gravitational acceleration ( $\Gamma > 1$ ) for the powder bed to detach from the base. Incidental airflow decreases the weight of particles so that detachment happens at  $\Gamma$ -values smaller than one. In this state, the powder bed is bouncing on the vibrating base with the same frequency, thereby periodically experiencing collisions with the base at the bottom reversal point and detachment at the top reversal point. When colliding with the base, kinetic energy is transferred to the powder particles and shock waves propagate through the powder bed. Agitation by vertical vibration effectively lowers the minimum fluidization velocity. When a bubbling bed is established at constant flow rate, the bubbling rate and hence aerosol generation can therefore be enhanced by increasing the vibration intensity.

De-agglomeration of powder particles is another aspect that must be considered for aerosol generation. The number of particles small enough to be released would decrease over time without the continuous generation of new particles by fragmentation of agglomerates. In short, we presume different mechanisms responsible for the de-agglomeration of particles of HAR materials. When powder particles collide with the base and with each other, they might be subject to fragmentation when the elastic energy that dissipates by deformation outweighs the internal binding energy of the agglomerates. The agglomerates shown in Fig. 1 have surface features that might be subject to two different mechanisms of de-agglomeration. Firstly, individual fibres attaching and smaller agglomerates sticking to the agglomerate surface might be more escapable, since their binding energy is much lower [46]. They can be liberated by an abrasion-like strain, when agglomerates collide and scrape past each other and the container walls. Secondly, parts of agglomerates can be chipped off. Agglomerates are non-spherical, often exhibiting surface features like edges and extensions. It is considerable that protrusions break away more easily from the agglomerate due to increased strain [47]. Fragmentation of individual nanotubes was assumed improbable.

In conclusion, aerosol generation with the fluidizer is achieved by a bubbling fluidized bed, perceptible by bed height extension and frequent ejections of powder at the bed surface. Vibrational agitation not only facilitates fluidization by breaking up entanglements of agglomerates and fibres but also generates fresh particles by de-agglomeration for continuous aerosol generation. A constant bubbling and therefore powder transport rate might result in a stable rate of aerosol generation, observable by a stable particle number concentration.

## 2.3. Experimental setup

Fig. 2 shows a scheme of the experimental setup used in all experiments presented in this paper. A multi-purpose solenoid magnet ‘vibration test system’ (type TV 52110, TIRA GmbH, Schalkau, Germany), the ‘shaker unit’, was used to generate periodic vertical displacement of mechanically connected parts by means of applying alternating

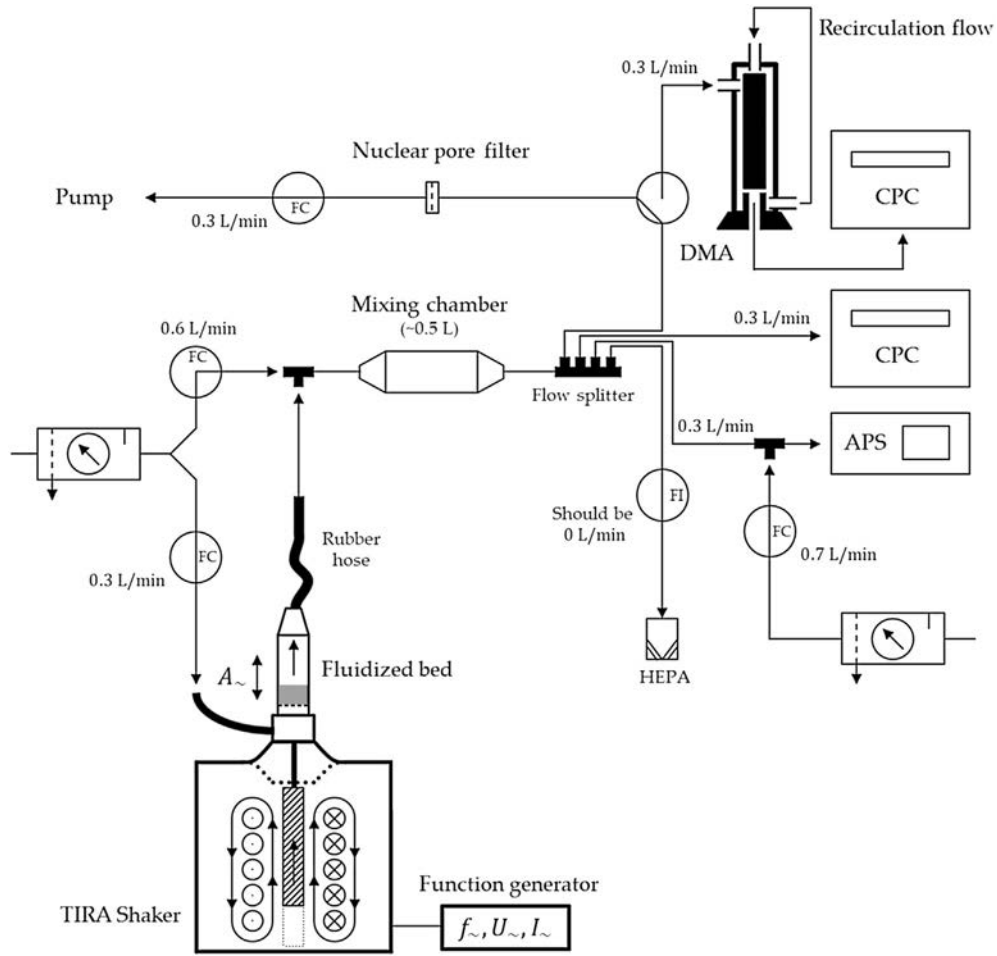


**Fig. 2.** Scheme of the experimental setup of the dustiness test with the fluidizer. Abbreviations: FC – mass flow controller, FI – mass flow indicator, DMA – differential mobility analyser, CPC – condensation particle counter, APS – aerodynamic particle sizer.

electromagnetic forces on an ferromagnetic piston connected to a platform supported by rubber bands. The vertical displacement amplitude  $A$  was measured with a laser rangefinder (type HL-G108, Panasonic Electric Works SUNX) with  $2.5 \mu\text{m}$  resolution and 5 kHz maximum frequency. The amplitude  $A$  was controlled and adjusted via the sinusoidal supply voltage of the solenoid magnet. This setup could theoretically generate vertical vibrations within a wide band of frequencies. Higher frequency required stronger voltages to maintain certain amplitudes, depending on the weight of the shaken body.

Fig. 3 shows a schematic sectional drawing of the sample test tube holder that was mounted on the piston's platform and aligned perpendicular to the ground floor in an upright position. It was constructed entirely of ISO-KF (DN25 and DN16) vacuum components of  $r = 12.5 \text{ mm}$  inner radius, tapered to 8 mm at the upper end. The sample powder

material was placed on a circular sheet of a filter fabric of twilled Dutch weave with 12.5 mm radius and  $1 \mu\text{m}$  pore size made from AISI 1.4401 stainless steel. A cellulose filter of the same radius mechanically supported the filter fabric. Both filters were clamped with two O-rings to the bottom gasket with the metal fabric facing up.

The inlet was connected to the gas supply using a push-in tube fitting (Parker). The aerosol outlet comprised of a Swagelok™ compression fitting with an 8 mm steel tube. Using a conductive silicon hose it was connected to an 8 mm tube tee connector at which the sample flow with a volumetric flow rate of  $Q_v = 0.3 \text{ slm}$  was diluted with 0.6 slm particle-free air. Both, sample flow rate and dilution flow rate, were maintained by mass flow controllers (FC) (type “red-y smart”, Vögtlin Instruments GmbH, Aesch, Switzerland). The resulting flow of 0.9 slm was led to a small stainless steel mixing chamber (also made

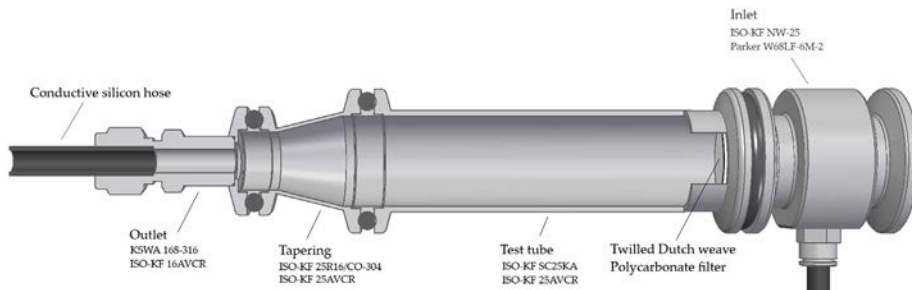


**Fig. 3.** CAD-model of the sample test tube.

of ISO-KF parts) of 0.5 L volume and was then split for the connecting instruments. These comprised (1) a stand-alone condensation particle counter (CPC, type 5.403, GRIMM Aerosol Technik Ainring GmbH & Co. KG, Ainring, Germany), (2) a GRIMM Scanning Mobility Particle Sizer (SMPS, type 5.403) with a Vienna-type long differential mobility analyser (DMA, type 55–900) and (3) an aerodynamic particle size spectrometer (type APS 3321, TSI GmbH, Aachen, Germany). Both, CPC and SMPS, require a flow rate of 0.3 slm whereas the APS uses a flow rate of 1.0 slm for which a second dilution state with a flow rate of 0.7 slm was implemented. This setup resulted in the sample flow being split into three equal parts of 0.3 slm for each instrument. The CPC counted all emitted particles smaller than approximately 3 µm with a temporal resolution of 1 s. The SMPS measured the electrical mobility size distribution within a size range of 10–1000 nm. One scan required approximately 7 min. The APS measured the aerodynamic size distribution within a size range of ca. 0.5–20 µm every minute.

A filter setup was used to collect aerosol samples. It comprised a PGP sampler, a flow controller for a sampling flow rate of 0.3 slm and a pump. Gold-coated polycarbonate track-etched membrane filters with a diameter of 37 mm and 200 nm pore size were used. The filters exhibit a collection efficiency better than 99% for CNT aerosols, as was determined in a previous study on personal samplers for CNT dusts [48].

An additional mass flow indicator (FI) (type 4143, TSI GmbH) was connected to the flow splitter to detect possible flow inconsistencies. Particle-free pressured air with <2% relative humidity was used for sample flows and dilution flows for all experiments.

#### 2.4. Energy input by the fluidizer

The fluidizer's energy input to the powder measured as power  $P$  can be calculated as the change of the powder's kinetic energy per second. We consider only the energy transfer by the vibrating base that happens uniformly over the cross-section of the powder bed due to the symmetry of the sample test tube (see next section). Per second, the base collides with the powder bed depending on frequency  $f$ . Energy is transferred with each collision depending on the kinetic energy  $W$  of the powder bed with mass  $M$ :

$$P = Wf = \frac{1}{2}M v_f^2 f = 2\pi^2 M A^2 f^3, \quad (2)$$

where  $v_f = 2\pi A f$  is the average velocity of the base.

**Table 2**  
Operational conditions and measurands for the shaker test procedure.

Operational parameter	Symbol	Value	Comment
Sample flow rate	$Q_{VF}$	0.3 slm	
Frequency	$f$	30 Hz, 50 Hz	Applying Eq. (1) results in respective vibration intensities $\Gamma$ of 1.8 and 5
Displacement amplitude	$A$	0.5 mm	
Powder mass	$m$	300 mg	
Duration	$T$	>90 min	Data evaluation range 15–75 min after starting aerosol generation
Measurand of aerosol monitoring			
Particle number concentration	$n_i$	#/cm <sup>3</sup>	$i$ = CPC, SMPS, APS
Number-based dustiness index	$I_{CPC}$	#/mg	In the approx. Size range 10–3000 nm (CPC)
Emission rate	$E_{CPC}$	#/mg/s	In the approx. Size range 10–3000 nm (CPC)
Number of size modes	$N$	–	Of the time-averaged combined size distributions of SMPS and APS
Modal diameters	$d_N$	nm	The highest and second highest mode
Measurand of morphological characterization			
Individual fibre fraction	$w_f$	%	Percentage of an ensemble of 500 particles, after applying counting rules.
Fibrous agglomerate fraction	$w_{fa}$	%	
WHO-fibre fraction	$w_{WHO}$	%	
Spheroid agglomerate fraction	$w_{pa}$	%	
Impurity fraction	$w_i$	%	
Length range	$L$	µm	Median
Diameter range	$d$	nm	Median

#### 2.5. Dustiness testing procedure and measurands

In the following, we describe the operation procedure for dustiness testing of HAR materials with our fluidizer setup. Prior to deciding on specific test parameters, different vibration frequencies, amplitudes, flow rates as well as powder masses were studied with regards to fluidization and particle number concentration behaviour. The comparison of results allowed finding a parameter set that is suited for stable aerosol generation for a wide range of MWCNT materials. These preliminary tests are described in the first part of the Results section. Table 2 summarizes the operational parameter used throughout this paper.

Each dustiness test was repeated three times for each material with the same set of operational conditions. For these three dustiness tests, three aluminium vials were filled with 300 mg of sample powder each and stored in a desiccator for at least 24 h to lower the materials humidity before usage. The sample test tube was disassembled in a glovebox and thoroughly cleaned. A new steel filter fabric was used for each test. After reassembling the sample test tube without connecting the tapered upper end, the powder was poured on the steel filter fabric and the sample test tube closed. The test line was situated in a workbench protecting the user from unintended particles emissions. In addition to thoroughly cleaning all parts of the assembly prior to the dustiness test, the test system was perfused with particle-free compressed air for ca. 15 min to cleanse the test line from residue particles.

To start the experiment, the first dilution side stream flow rate was set to 0.9 slm, the sample flow rate was set to zero and the monitoring instruments were turned on. For the duration of at least 14 min (two SMPS scans), the particle number concentration had to be lower than the measurement error of the CPC (about 10 #/cm<sup>3</sup>). In parallel, the sample test tube containing the test materials was attached to the platform of the shaker unit, grounded, adjusted perpendicular to the ground and connected to the rubber hose. The shaker unit was switched on and the sample flow rate was set to 0.3 slm the moment a new scan of the SMPS system started. The first dilution side stream was set to 0.6 slm, accordingly. Following the start of aerosol generation, the system was unchanged for at least 90 min. Afterwards, the shaker unit and the sample flow rate were switched off. Table 2 summarizes all measurands of the fluidizer that were obtained by the aerosol monitoring.

For one of three repeated dustiness tests, the SMPS was exchanged with the filter sampling equipment as described above. Particle collection started the moment the shaker unit and sample flow rate were switched on and particles were collected for 75 min. The filters were analysed using a scanning electron microscope (SEM, type SU8230, Hitachi High-Technologies GmbH, Krefeld, Germany) that

was operated at a magnification of 3000, which resulted in a pixel size of 8.3 nm for  $5120 \times 3840 = 20$  Megapixel SEM images. This magnification was chosen because initial tests showed that individual CNTs with the smallest diameters (SMW 100) could be visualized at this pixel resolution while keeping the image area ( $31.7 \mu\text{m} \times 42.3 \mu\text{m} = 1344 \mu\text{m}^2$ ) large enough to fully display the longest fibres (MWCNT-7). The lower resolution limit of the SEM was therefore 8.3 nm. SEM images were taken at random filter sample locations. The number of SEM images taken correlated with the number of particles detected/found on the filter, to cover >500 particles. The minimal number of SEM images required to meet this number was estimated from the average particle number concentration measured during the dustiness test with the CPC, assuming homogenous deposition density on the filter.

Dustiness tests were performed for each material at two different vibration intensities,  $\Gamma = 1.8$  and  $\Gamma = 5$ , corresponding to  $f = 30$  Hz and 50 Hz, respectively, while maintaining an amplitude of 0.5 mm. Applying Eq. (2), the fluidizer agitated 300 mg powder with a power of 40  $\mu\text{W}$  and 185  $\mu\text{W}$ , respectively.

## 2.6. Counting rules

For each filter sample collected during the fluidizer test, at least 500 of the particles that were identified on SEM images were morphologically classified and counted. Only particles that were fully contained in an image were counted and characterized. A set of counting rules defined the different morphological classes of objects as well as how individual fibres were measured to determine length and diameter. Particles were divided into the following five subclasses. Fig. 4 shows examples of members of these morphological classes that were found on filter samples from tests with the material ARIGM001.

1. Individual fibres with an aspect ratio of  $>3:1$ .
2. Fibre-shaped fibre agglomerates with an aspect ratio of  $>3:1$ , as shown in Fig. 4(b)

3. Individual fibres and fibre-shaped agglomerates matching WHO-geometry, as shown in Fig. 4(a). This class is a subclass of class 1 and 2
4. Particle-shaped fibre agglomerates with an aspect ratio smaller than 3:1, as shown in Fig. 4(c).
5. Particles with an aspect ratio smaller than 3:1 that are neither fibres nor composed of fibres are called impurities.

For individual fibres, lengths and diameters were measured. For fibrous agglomerates, the length of the outer shape was determined and the diameter estimated based on the assumption of a mean diameter. Note that our image analysis routine provides correlated pairs of diameter and length for fibres as well as fibrous agglomerates.

Note, that specific particles allocated to group one and two make group three. This was decided because the criteria for hazardous fibres by the WHO (see introduction) does not differentiate between individual fibres and agglomerates. In the remainder of this paper, we use the abbreviation “WHO-fibre” for all particles belonging to group three. Clusters of fibres that comprised only few and individually identifiable fibres/particles were not classified as agglomerates (group 2 and 4) but as individual fibres (group 1). This appeared most often in intersecting fibres on the images. Fibres were regarded “identifiable” when their ends could be assigned. In some cases, two or more classes formed a connected object. Their grouping was decided upon its enveloping outer shape. An example is given in Fig. 4(d), a fibrous agglomerate sticking out of a spheroidal agglomerate. The fibrous agglomerate cannot be individually counted since it disappears in the agglomerate. Here, the object belonged to the groups two and three, since the overall shape was fibrous and matched the bounds of the WHO-geometry.

Morphological characterization was performed using image processing software tools. For the samples collected at  $\Gamma = 5$  and evaluated first, GNU Image Manipulation Program (GIMP) was used. This study coincided with the development of a specialized program for SEM image analysis for the morphological characterization of fibre dust particles. This software called ‘Fibre Analysis Tool’ was used for the

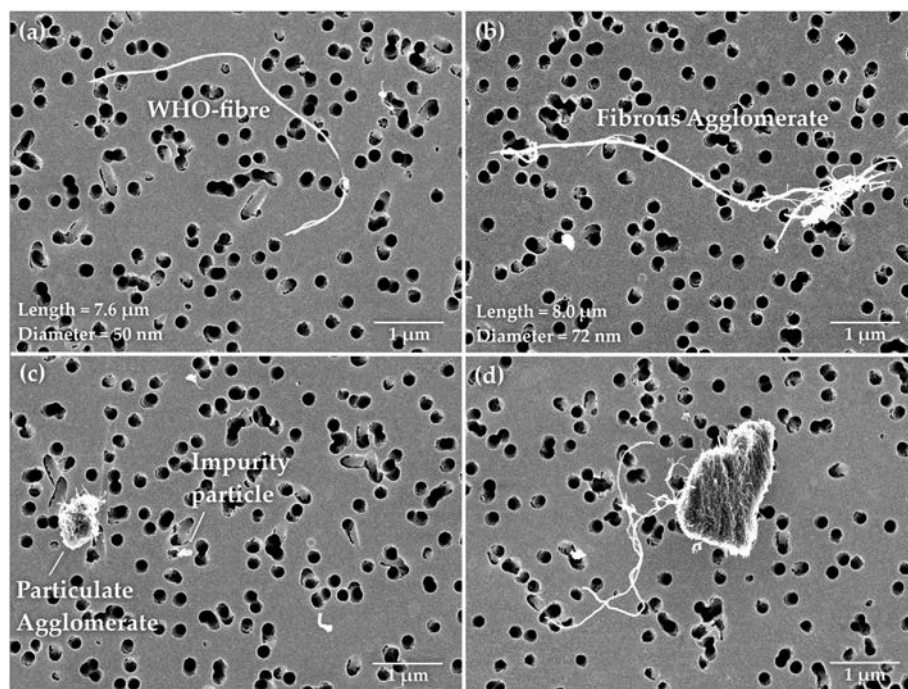


**Fig. 4.** SEM images of dust particles of ARIGM001, collected on a track-etched membrane filter when the fluidizer was operating with vibration intensity 1.8. The four images display the morphological classes of objects found on the filter, which were individual fibres which in the case of (a) was identified as an WHO-fibre, MWCNT agglomerates with an outer shape matching WHO-criteria (b), spherical MWCNT agglomerates like in (c) on the left side and nanoparticles that are clearly not CNTs as visible in (b), (c) and (d). Some particles like in (d) are a hybrid between two morphological classes.

evaluation of the  $\Gamma = 1.8$  samples. Both programs worked with equivalent techniques, namely acquiring the pixel length of a Bezièr-spline-interpolated path tracing the shape of a fibre. We therefore consider results obtained with both programs as comparable. The spline length in pixels was translated into the geometric fibre length in nanometres. The fibre diameter was measured similarly by applying the path length determination tool across the fibre.

A number of errors could occur due to subjectivity and limitations by the image acquisition. For once, the ruling for identifiability stated above was based on subjective certainty, which could lead to different decisions when counting a cluster of fibres as an agglomerates or each fibre by itself. In addition, connected particles of different classes were sometimes counted individually, even though one or more particles were not fully displayed. In addition, since the pixel size was 8.3 nm, the diameters of Baytubes 150P, NC7000, NM400 and SMW 100 appeared only along one or two pixels in the images due to their thinness. Sharpness was lacking, possibly leading to an overestimation of the diameter when the image zoom during tracing was not optimal.

### 3. Results

Both vibration and aeration parameters were systematically studied in terms of fluidization behaviour and aerosol generation. The general ability of the fluidizer to generate fluidized beds is tested in dependence of the three control parameters: frequency, amplitude and flow rate. In parallel, temporal behaviours of the particle number concentration for different fluidizer conditions are discussed, seemingly characteristic for different fluidization states. Our aim was to find a set of control parameters in order to achieve equivalent fluidization conditions for the majority of the 15 materials, enabling a dustiness testing with high comparability.

#### 3.1. Fluidizer optimization

In the following, we describe our observations of changes in powder bed behaviour at different fluidizer settings, i.e. sample flow rate and vibration frequency as well as amplitude. This required replacing the conductive aluminium main cylinder with a cylinder made from borosilicate glass for visibility. In parallel, we monitored the particle number concentration with the CPC. We considered similarity of powder bed behaviours as a criterion for the comparability of the dustiness tests. We presumed that equivalent fluidization behaviour would also cause an equivalent aerosol generation mechanism, providing qualitatively equivalent time-dependencies of the particle number concentration curves. Linking characteristic concentration curves with the powder bed behaviour was important because the latter was not observable in the actual dustiness tests.

Four powder bed states were observed during the performance tests: (i) the initial packed bed when shaking and sample flow rate were turned off, (ii) gas by-passing by channelling, (iii) the powder bed expansion in volume and continuous ejections of powder particles and (iv) formation of large clods that bounced on the powder bed surface while smaller particles were still ejected. Observation of bed extension and powder ejections is in accordance with the considerations made earlier that MWCNT-powders would show bubbling fluidized bed properties. Unfortunately, bubbles themselves could not be visibly observed, because they tend to rise near the center of the powder bed [41].

Fig. 5 shows the particle number concentration measured with the CPC while changing the control parameters of the fluidizer. In Fig. 5 (a), the frequency was changed, in (b) the amplitude and in (c) the sample flow rate while upholding the settings of the respective other parameters. Results with ARIGM001 are shown here exemplarily. Results for the frequency dependency are also available for ARIGM002, Baytubes C150P, CNTMW, NM400, NM401 and NTX-3, showing qualitatively equivalent results except NM401. When increasing the frequency,

the concentration visibly increased with each step. For 10 Hz and 20 Hz, the particle concentration dropped back to the background level afterwards. The powder bed showed no volume expansion but channelling (state (ii)). At 30–50 Hz, the particle number concentration kept a constant level. A volume expansion was visible by a small increase of the bed height. Particles were ejected upwards (state (iii)). At 60 Hz, the particle number concentration was fluctuating. Here, mm-sized clods formed and bounced on the bed surface (state (iv)). NM401 showed no powder bed volume expansion at any frequency settings. Instead, channelling was observed upon changing the frequency accompanied by a concentration peak. At 50 Hz and beyond, particles were bouncing on the powder bed surface with sizes in the mm-range. The particle number concentration then fluctuated strongly and showed an increasing trend.

Fig. 5(b) demonstrates that increasing the amplitude also resulted in a higher level of stable particle number concentration. A small bed volume expansion was observed also at lower amplitudes of ca. 0.35 mm, accompanied with particle ejection at the bed surface.

In Fig. 5(c), stable particle number concentration set in already at the lowest sample flow rate of 0.1 slm. However no bed volume expansion was observed until the flow rate was changed to 0.3 slm. Interestingly, further increase of the sample flow rate would not lead to significant changes in the particle number concentration. However, powder beds extended further with increasing flow rates. At 1.0 slm, a decrease was observed accompanied with the establishment of moving mm-sized voids and agglomerates, visible at the walls of the sample test tube.

In conclusion, ARIGM001 showed fluidized beds and plateaus of the particle number concentration for  $f = 30 - 50$  Hz (with  $A = 0.5$  mm and  $Q_v = 0.3$  slm),  $A = 0.35 - 1.5$  mm (with  $f = 30$  Hz and  $Q_v = 0.3$  slm) and  $Q_v = 0.3 - 1.0$  slm (with  $f = 30$  Hz and  $A = 0.5$  mm). Particles were ejected from the powder bed surface due to bubbling which contributed to aerosol generation. For this reason, it was decided to run the dustiness tests with frequencies of 30 and 50 Hz and amplitude of 0.5 mm, corresponding to vibration intensities of  $\Gamma = 1.8$  and  $\Gamma = 5$ . Because powder bed extension occurred at  $Q_v = 0.3$  slm and higher flow rate further would not lead to higher particle number concentration, we chose this value as the standard sample flow rate.

We also determined the vibration intensities at which a fluidized bed formed by tuning the frequency with smaller step size than in den previous measurements, while maintaining the amplitude at  $A = 0.5$  mm and the sample flow rate at  $Q_v = 0.3$  slm. We performed this test for all 15 materials. For 13 materials, the vibration intensities at which a fluidized bed was established were in the range of  $\Gamma = 0.3 - 0.8$  for powders with tap densities lower than  $0.1$  g/cm<sup>3</sup> and  $\Gamma = 0.7 - 1.8$  for higher tap densities (see Table 1). MWCNT-7 and NM401 could not be fluidized under any set of parameters tested.

Changing powder mass  $M$  was expected to directly influence the average particle number concentration as more powder particles would increase the probability of aerosol release. A series of dustiness tests with 50 mg, 100 mg, 200 mg and 500 mg of the materials ARIGM001, Baytubes C150P, CNT-MW and NM400 was conducted with vibration intensities  $\Gamma = 1.8$  and  $\Gamma = 5$  and a sample flow rate of 0.3 slm. The resulting average particle number concentrations increased linear with the powder mass in all cases and non-linear with saturation at powder masses larger than 200 mg in case of  $\Gamma = 5$  for ARIGM001 and CNT-MW. A graph summarizing these results is presented as supplementary information for this paper. When performing dustiness tests for material comparisons, a powder mass of 300 mg was used for all materials except for MWCNT-7 and NM401 where 150 mg were used because of low tap densities. At this test mass, the amount of material was sufficient to establish a fluidized bed with the bed expansion not reaching the tapered part of test tube.

Finally, additional tests showed that fluidized powder beds showed good stability of the particle number concentration for more than 2 h of operation.

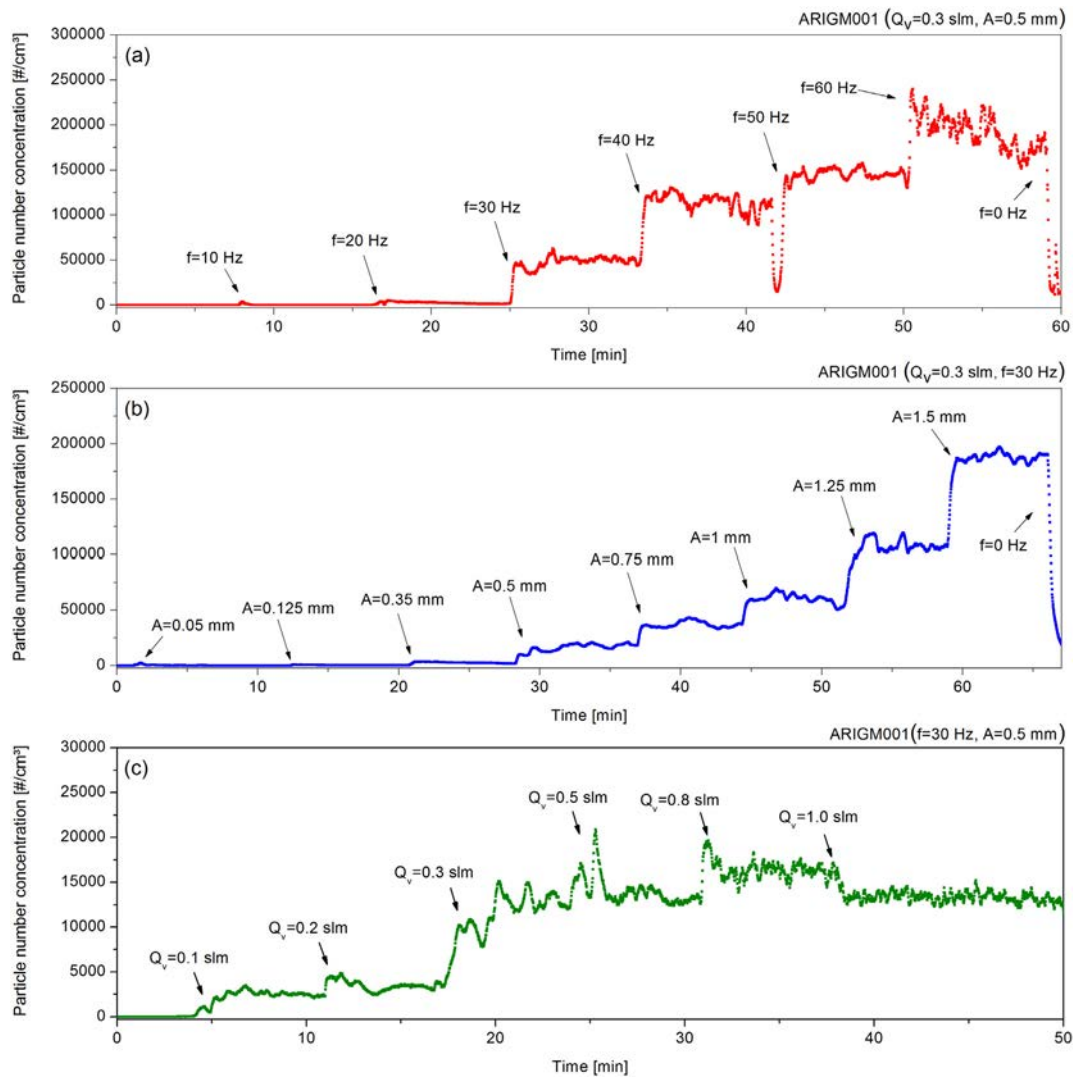


**Fig. 5.** Three CPC-measurements of the particle number concentration during aerosol generation with ARIGM001, when stepwise changing one control parameter of the fluidizer while keeping the others constant. In (a), the frequency was changed, while maintaining  $A = 0.5$  mm and  $Q_v = 0.3$  slm. In (b), the amplitude was increased while keeping  $f = 30$  Hz and  $Q_v = 0.3$  slm constant. In (c), the sample flow rate was adjusted while upholding  $f = 30$  Hz and  $A = 0.5$  mm.

### 3.2. Dustiness tests

The procedure for the dustiness test described in Section 2.5 was decided upon the results of the fluidizer performance tests and applied to the 15 MWCNT materials in Table 1.

Fig. 6(a) shows the CPC data of the three runs of the dustiness test with C2154 when the fluidizer was operated at  $\Gamma = 1.8$ . For most materials, such concentration measurements were reproducible. The particle number concentration seemed to be stable after a period of increase following the start of the shaker unit at the 14 min mark. The time required to reach stable aerosol generation was between 5 min and 15 min, with stability occurring more quickly with the higher vibration intensity. To determine dustiness measurands like average particle number concentration, it was decided to use only data points during stable particle number concentration, i.e. data ranging from 15 to 75 min after the start of aerosol generation (1 h). The energy inputs were 0.18 W and 0.83 W for  $\Gamma = 1.8$  and  $\Gamma = 5$ , respectively.

At  $\Gamma = 5$  the particle number concentration was also stable except for Baytubes C150P, MRCSD, MWCNT-7 and NM401. The particle number concentration of MWCNT-7 and NM401 decreased asymptotically towards the background level, as shown in Fig. 6(b). For one of the three runs, the particle number concentration showed a second peak

later in the dustiness test. Baytubes C150P and MRCSD at  $\Gamma = 5$  showed a peak upon start of aerosol generation. The concentration dropped slowly and did not reach the background over the duration of the dustiness test.

Table 3 summarizes the results on mean values of our measurands for dustiness from Table 2 that could be determined from aerosol monitoring with the CPC, SMPS and APS. The data points were linearly regressed with an error-weighted least-square fit considering a slope of zero to obtain an average value of the particle number concentration time series and its standard error. Unstable particle number concentrations like in Fig. 6 (b) are reflected by the high standard errors. The number-based dustiness coefficients  $I_{CPC}$  could be calculated using the data of the CPC:

$$I_{CPC} = \frac{Q_v}{M} \sum_{j=1}^{T/\Delta t} n_j, \quad (3)$$

where  $T$  is the duration of the evaluated fluidizer process (60 min),  $\Delta t$  is the time step between two subsequent data points  $n_j$  and  $n_{j+1}$ , and  $n_j$  are the concentration data points measured with the CPC. Average emission rates were given by the linear regression assuming zero slope for the mass-normalized mean number of particles emitted in

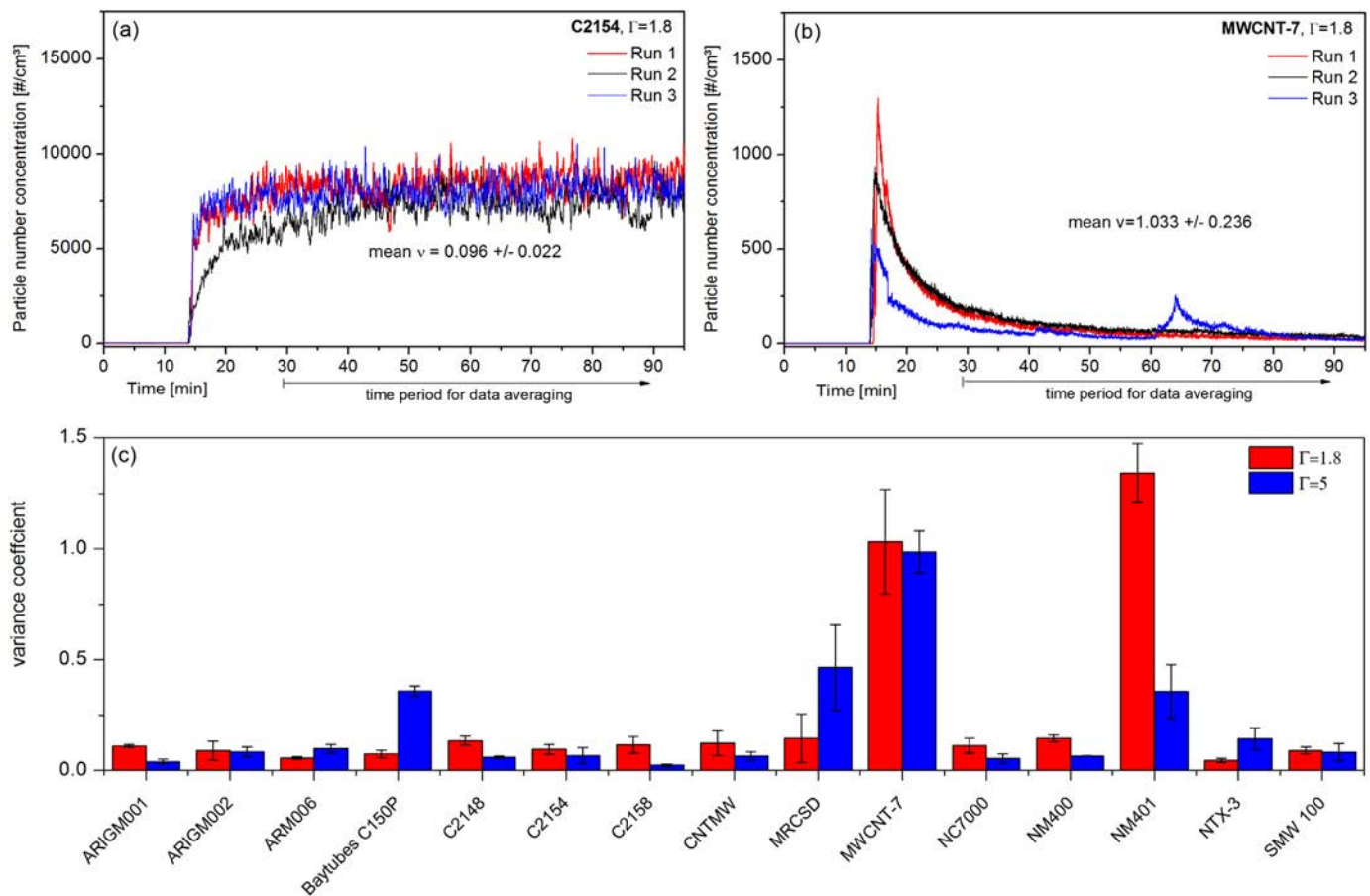


**Fig. 6.** Particle number concentrations as a function of time measured during the three dustiness test for C2154 (a) and MWCNT-7 (b) with the fluidizer operating with  $\Gamma = 1.8$ . Dustiness measurands were determined for the time period 15 min after starting the dustiness test for data covering 60 min of continuous measurements. The variance coefficient of the data range representing 60 min of continuous measurement with the CPC for  $\Gamma = 1.8$  and  $\Gamma = 5$  (c).

1 s, i.e. one data point measured by the CPC. Note that emission was not linearly dependent on powder mass. Consequently, all mass-normalized measurands are only valid for the applied powder mass of 300 mg (150 mg for MWCNT-7 and NM401).

Size distributions  $dN/d \log(N_{CMD})$  measured with the SMPS and APS were fitted with a lognormal distribution depending on the diameter  $x$ . This allowed to determine the position of the so-called count-median diameter  $x_{CMD}$ , i.e. the median of the number-based size statistic, the geometric standard deviation  $\sigma_g$  and the particle number concentration  $n$  [49]:

$$\frac{dN}{d \log(N_{CMD})}(x) = \frac{n}{\sqrt{2\pi} \log(\sigma_g)} e^{-\frac{(\log(x) - \log(x_{CMD}))^2}{2 \log(\sigma_g)^2}} \quad (4)$$

Fig. 6 shows the time-averaged size distribution of C2154, measured with the SMPS (10–1000 nm) and APS (0.5–20  $\mu\text{m}$ ), in a combined plot to allow for direct comparison. The size channels of SMPS and APS represent diameters of spheres that are equivalent on the basis of different physical parameters, electrical mobility and inertia. Therefore, the datasets of SMPS and APS are interpreted separately. The size distributions measured with the SMPS were mono-modal. In most cases, the APS showed a large peak at small aerodynamic diameters (0.5–1  $\mu\text{m}$ ) and for some materials a second, much smaller peak at higher diameters (1–3  $\mu\text{m}$ ). Note that the right flank of the first peak might be caused by the well-known decay of the number size distribution of the APS due to the less than a hundred percent counting efficiency in the smallest two or three size channels. Consequently, determination of e.g. its count median diameter must be regarded of limited value. The SMPS completed

one scan of the size distribution every 415 s. Therefore, over the course of 60 min, eight values for size, geometric standard deviation and particle number concentration were obtained. The geometric standard deviations were in the range of 1.4–1.8. Concentrations measured with the SMPS were 1.5 – 2 times higher compared to the values measured with the CPC at vibration intensities  $\Gamma = 1.8$  and 5, respectively. The size distributions did not change over the course of the time of the dustiness test. For the materials NM401 and MWCNT-7, the SMPS measured no comprehensible data, only occasional spikes in random channels. The mean aerodynamic diameter distributions measured with the APS were fitted with a two-peak lognormal distribution with the individual peaks described by Eq. 4.

### 3.3. Morphological characterization of track-etched membrane filter samples

Nine different persons evaluated the filter samples following equivalent counting and characterization rules, with different combinations of two persons for the assessment of each sample. In practice, more images were taken with the SEM than required according to the estimation based on the average particle number concentration. Which images one person was evaluating was determined randomly beforehand. Therefore, persons analysed different sets of images. Nevertheless, for most materials, the person-to-person variations of the sizes of the morphological class fractions were acceptably small, when also considering the error sources described earlier.

Table 4 summarizes the results on morphological characterization and geometric measurement of fibrous objects. The fractions of the different morphological classes are presented as percentages of the

**Table 3**

Particle number concentrations determined with each instrument, number-based dustiness index, emission rate, number of modi in the size distribution, 1st and 2nd mode of the size distribution.

Materials	n			$I_{CPC}$	$E_{CPC}$	N	$d_{(N)}$	
	[#/cm <sup>3</sup> ]	[#/cm <sup>3</sup> ]	[#/cm <sup>3</sup> ]				[#]	[nm]
Metric	[#/cm <sup>3</sup> ]	[#/cm <sup>3</sup> ]	[#/cm <sup>3</sup> ]	[#/mg]	[#/mg/s]		1st mode	2nd mode
$\Gamma = 1.8$	CPC	SMPS	APS					
ARIGM001	3656 ± 10	7351 ± 335	64.3 ± 1.0	115,436 ± 9068	32.1 ± 2.5	1	127.6 ± 1.5	–
ARIGM002	1222 ± 8	2115 ± 64	3.5 ± 0.1	35,959 ± 1818	10.0 ± 0.5	1	134.3 ± 1.5	–
ARM006	1186 ± 12	1486 ± 21	13.8 ± 0.1	37,006 ± 8978	10.3 ± 2.5	1	104.8 ± 2.2	–
Baytubes C150P	173 ± 1	216 ± 13	4.6 ± 0.1	5477 ± 1132	1.5 ± 0.3	1	107.4 ± 2.8	–
C2148	454 ± 4	821 ± 37	6.2 ± 0.1	14,145 ± 1258	3.9 ± 0.3	2	104.8 ± 2.2	1950 ± 10
C2154	7539 ± 44	10,757 ± 68	151.0 ± 1.1	222,487 ± 13,198	61.8 ± 3.7	2	132.8 ± 1.8	2020 ± 20
C2158	3947 ± 17	6778 ± 89	594.5 ± 5.9	119,715 ± 2446	33.3 ± 0.7	1	194.1 ± 3.0	–
CNT-MW	422 ± 6	657 ± 25	27.1 ± 0.6	12,621 ± 1870	3.5 ± 0.5	1	73.6 ± 2.1	–
MRCSD	478 ± 5	464 ± 34	207.9 ± 2.7	13,325 ± 2388	3.7 ± 0.7	1	331.8 ± 6.4	–
MWCNT-7	134 ± 7	–	64.2 ± 6.8	12,397 ± 2721	3.4 ± 0.8	1	–	500 ± 40
NC7000	204 ± 2	365 ± 22	16.1 ± 0.2	7495 ± 1496	2.1 ± 0.4	1	88.4 ± 4.6	–
NM400	179 ± 1	227 ± 21	9.1 ± 0.2	4441 ± 60	1.2 ± 0.1	1	66.3 ± 2.8	–
NM401	44 ± 3	–	25.8 ± 2.8	4441 ± 1854	1.2 ± 0.5	1	–	530 ± 20
NTX 3	8779 ± 54	14,276 ± 119	1309.5 ± 6.5	270,580 ± 54,709	75.2 ± 15.2	1	146.3 ± 3.2	–
SMW 100	204 ± 1	195 ± 1	1.8 ± 0.1	6247 ± 489	1.7 ± 0.1	2	76.2 ± 1.3	1490 ± 20
$\Gamma = 5$								
ARIGM001	23,466 ± 890	45,392 ± 669	441.4 ± 2.1	213,260 ± 5411	59.2 ± 1.5	1	126.3 ± 1.3	–
ARIGM002	5830 ± 29	9879 ± 120	13.2 ± 0.1	184,275 ± 38,510	51.2 ± 10.7	1	123.4 ± 1.2	–
ARM006	16,052 ± 101	34,146 ± 454	166.0 ± 0.9	456,886 ± 60,592	126.9 ± 16.8	1	94.8 ± 1.2	–
Baytubes C150P	1276 ± 23	1877 ± 124	14.9 ± 0.4	49,204 ± 2579	13.7 ± 0.7	2	79.2 ± 2.3	1720 ± 20
C2148	2569 ± 8	4328 ± 18	22.1 ± 0.1	79,967 ± 3652	22.2 ± 1.0	2	94.8 ± 1.2	2080 ± 20
C2154	20,951 ± 125	41,784 ± 248	377.4 ± 3.7	644,383 ± 38,696	179.0 ± 10.7	2	137.3 ± 1.8	2000 ± 140
C2158	22,614 ± 156	53,294 ± 596	2788.3 ± 19.5	713,527 ± 39,790	198.2 ± 11.1	1	170.7 ± 1.7	–
CNT-MW	2156 ± 9	2710 ± 41	307.0 ± 13.3	65,236 ± 2819	18.1 ± 0.8	2	68.5 ± 0.8	–
MRCSD	4850 ± 110	4027 ± 425	1898.4 ± 87.3	193,635 ± 11,694	53.8 ± 3.2	1	301.4 ± 7.6	–
MWCNT-7	463 ± 22	–	138.6 ± 12.5	31,783 ± 1402	8.8 ± 0.4	2	–	500 ± 20
NC7000	1726 ± 6	2266 ± 42	62.6 ± 0.3	56,711 ± 7406	15.8 ± 2.1	2	66.4 ± 1.5	–
NM400	578 ± 72	1450 ± 37	43.0 ± 0.5	24,560 ± 316	6.8 ± 0.1	2	66.7 ± 1.75	–
NM401	721 ± 13	–	231.3 ± 9.5	35,826 ± 6042	10.0 ± 1.7	2	–	590 ± 20
NTX 3	27,953 ± 216	26,962 ± 1465	3704.4 ± 43.6	825,397 ± 276,222	229.3 ± 76.7	1	147.0 ± 2.6	–
SMW 100	2768 ± 19	6403 ± 39	17.1 ± 0.4	84,865 ± 9123	23.6 ± 2.5	2	74.5 ± 0.9	1600 ± 30

entirety of particles found on the filter. Note that some particles were allocated to two classes, counting as WHO-fibres while being individual fibres or fibrous agglomerates. Due to the subjectivity of the assessment, no mean values are presented, but the results of each individual evaluation. Some powders proved to be polydisperse, being mixtures of either two different nanotubes or nanotubes and fibrous contaminants. Fibrous contaminants were rare in numbers except for MRCSD, where different types of carbon fibres were present in large numbers. In most cases, the fraction of individual fibres was by far the largest. The numbers of larger objects in form of agglomerates were small. This explains why the APS detected only a small fraction of particles. The second largest fraction was in most cases impurities, not matching the purity grades stated by the manufacturers.

Note that since aerosol sampling started when the shaker unit and sample flow was switched on, the sampling time was not coincidental with the evaluation time of aerosol monitoring, since it was decided only later to use the time of stable concentration to determine dustiness. We thereby did not extrapolate particle number concentrations from the particle counting results. However, we assumed that the morphological distribution of the aerosol did not change significantly in the stabilization period. For future dustiness tests though, collection and data evaluation time should be matched.

The lengths and diameters of the studied MWCNT materials are given in Table 4 as the count based median values of the respective statistic ensemble. The errors were calculated according to ISO 13322-1 [50]. For the calculation, a lognormal distribution was assumed and statistically validated by a Kolmogorov-Smirnov test. It was found that the lengths as well as the diameters exhibit a lognormal distribution whereas a normal distribution was dismissed by the test. The errors of the medium diameter were calculated on a level of significance of 95%. The relative error depends on the number of fibres counted as well as

on the width of the size distribution in the material. Most materials exhibit a geometric standard deviation of the length of about 2.0–2.4, while the geometric standard deviations of the diameter distributions were in the range 1.3–1.7. For the length distributions, relative errors of 8–14% resulted (except from Baytubes C105P, NC7000, NM400, NM401 with  $e > 20\%$ ). The relative errors for the diameters were about 3–7% (except from Baytubes C105P, NM401 with  $e \sim 10\%$ , NC7000, NM400 with  $e > 20\%$ ). The large errors obtained for the length distribution is a result of the relatively low number of fibres counted, while the length distribution being wide at the same time. This is especially true for materials that released small number of individual fibres (see discussion below). In order to reduce the error to <5% for a distribution with a geometric standard deviation of 2.4, >1000 fibres have to be counted.

#### 4. Discussion

The observation of different powder bed states accompanied with characteristic time-dependencies of the particle number concentration that were dependent on the fluidizer control parameters motivate a closer look into the mode of aerosol generation, achievable with the experimental setup. We used aerosol monitoring and characterization not only to determine measurands of dustiness but also to characterize the aerosol quality generated by the fluidizer in terms of temporal number concentration and size stability. In addition, the responses of the aerosol monitors to aerosols emitted by MWCNT powder during the vibrofluidization are critically discussed in order to determine the validity of the measures stated in Table 2.

The essence of our application of the fluidizer is a material dustiness ranking of 15 different types of MWCNTs. It is based on the released total average particle number concentrations, of individual fibres and

**Table 4**  
Percentages of identified morphological classes and measured mean length and diameters of individual fibres after analysing track-etched membrane filter samples taken at vibration intensities of 1.8 and 5 by means of scanning electron microscopy. Total percentage is above 100% due to The WHO-fibres being allocated also to either individual fibres or fibrous agglomerates. P - Person that generated the respective dataset.

Material	P	Fibrous objects			Particulate objects		Length	Diameter
		Individual Fibres	Agglomerates	WHO-fibres	Agglomerates	Impurities	Median	
		$w_f$ [%]	$w_{fa}$ [%]	$w_{WHO}$ [%]	$w_{pa}$ [%]	$w_i$ [%]	$L$ [ $\mu$ m]	$d$ [nm]
$\Gamma = 1.8$								
ARIGM001	1	56.2	0.8	0.2	2.6	40.4	0.68	27
	2	60.1	1.7	0.4	11.1	27.2	0.72	33
ARIGM002	3	61.3	0	0	0.1	38.5	0.62	32
	1	55.7	1.4	0	0.2	42.8	0.56	31
ARM006	3	71.7	2.9	1.3	1.9	23.5	0.48	25
	4	60.5	8.8	1.3	7.0	23.7	0.41	25
Baytubes C150P	5	27.4	0.6	0	4.6	67.3	0.34	17
	3	20.2	0	0	0.6	79.2	0.56	8
C2148	4	47.5	1.0	0	5.7	45.8	0.26	12
	5	33.0	3.3	0	5.9	57.8	0.28	15
C2154	3	75.8	2.8	0.7	2.5	18.9	0.65	33
	6	71.2	2.0	0.4	11.0	15.9	0.59	34
C2158	1	82.9	3.8	1.8	13.3	0	0.96	41
	2	81.3	0.7	1.5	4.1	14.1	0.99	50
CNT-MW	7	75.4	0.4	0.2	6.4	17.8	0.38	12
	4	69.6	0	0.2	3.0	27.4	0.39	12
MRCSD	2	72.0	2.6	16.1	8.9	16.5	2.12	197
	7	58.1	16.1	10.2	9.7	16.1	2.02	126
MWCNT-7	2	81.4	2.7	8.4	6.4	9.5	1.83	83
	5	59.8	5.7	11.4	12.6	22.0	2.24	77
NC7000	5	5.8	0	0.2	2.0	92.2	0.63	21
	1	10.8	0	0	1.4	87.8	0.66	19
NM400	2	47.4	0.9	0.9	3.5	48.2	0.53	33
	5	25.0	0.9	0.4	4.4	69.7	0.43	18
NM401	3	25.0	0.9	8.2	2.4	71.8	3.69	66
	5	22.8	1.1	6.3	2.7	73.4	3.41	66
NTX 3	4	42.1	2.4	0.2	40.3	15.2	0.69	30
	2	41.7	1.8	0.2	41.9	14.6	0.62	42
SMW 100	3	63.4	0.6	0	0.2	35.7	0.40	17
	2	61.1	0.4	0	1.0	37.5	0.36	21
$\Gamma = 5$								
ARIGM001	1	54.7	3.0	0.1	6.7	35.6	0.71	29
	3	40.4	0	0.3	13.0	46.6	0.79	24
ARIGM002	8	86.4	0.2	0	0.4	13.1	0.56	32
	2	81.8	0	0	0.5	17.6	0.58	44
ARM006	8	71.1	0.8	0.4	6.9	21.2	0.49	25
	2	61.3	6.6	0.5	3.9	28.1	0.48	39
Baytubes C150P	8	63.8	0	0	2.8	33.4	0.38	20
	2	69.8	0.2	0	2.0	28.0	0.39	19
C2148	8	54.3	0.8	0	8.1	36.8	0.36	13
	7	61.6	4.3	0.2	13.2	20.8	0.31	21
C2154	4	81.4	1.5	0.8	8.2	8.9	0.56	36
	2	80.4	2	0.4	4.5	13.1	0.61	44
C2158	3	77.7	0.9	2.7	2.9	18.6	1.36	44
	8	80.7	1.6	1.1	5.5	12.1	0.91	45
CNT-MW	8	68.2	0	0	2.7	29.1	0.39	22
	2	70.2	1.4	0.2	2.2	26.1	0.48	29
MRCSD	3	55.4	1.9	5.1	2.6	40.1	2.21	141
	2	58.7	4.7	4.5	4.7	31.8	1.84	184
MWCNT-7	3	68.3	6.2	24.3	6.6	18.9	3.19	77
	2	71.4	5.6	13.0	10.5	12.5	1.98	93
NC7000	3	63.7	0.4	0	14.6	21.4	0.40	17
	1	60.2	9.5	0	7.4	22.9	0.39	16
NM400	9	55.4	1.2	0.8	2.5	41.0	0.44	14
	3	69.7	0.2	0.6	2.6	27.6	0.40	23
NM401	8	79.2	1.5	17.4	13.5	5.7	2.18	80
	2	72.5	4.2	18.8	13.8	9.5	2.52	95
NTX 3	8	48.5	0.3	0.3	44.2	7.0	0.54	34
	2	51.4	2.1	0.4	31.7	14.8	0.63	40
SMW 100	1	83.3	3.2	0	1.6	11.9	0.44	16
	3	83.0	1.7	0	0.6	14.7	0.50	16

WHO-fibres. The morphological characterization generated valuable data that allowed extracting information on health-relevant dust fractions from the datasets of the aerosol monitors. Based on the present study, we give recommendations for an optimized application of the fluidizer.

#### 4.1. Aerosol generation

Based on the observations during the fluidizer performance tests and dustiness tests, this section broadens the discussion of the aerosol generation mechanisms in the fluidizer that was described in

**Section 2.2.** As described earlier, aerosol generation is ultimately dependent on the amount of material that the bubbling fluidized bed supplies for aerosolization at its surface, determined by (i) disentanglement of powder particles, (ii) particles being transported and ejected by bubbles and (iii) liberation of individual fibres and agglomerates by de-agglomeration generating continuous supply of aerosolizable particles.

During the dustiness test, we observed a steady increase of the particle number concentration until signal stabilization sets in, as can be seen in Fig. 6 (a) for C2154. We presume that this period was required to gradually break entanglements between powder agglomerates in order to establish a fluidized bed. With disentanglement being more effective at the higher vibration intensities, this period was shorter at  $\Gamma = 5$ .

The rate of mass being transported as wake by bubbles is dependent on bubbling flow rate and the bubble size. In the fluidizer, the minimum fluidization velocity decreases in the process of powder bed disentanglement, leading to increasing bubbling flow rate and bubble size [36]. Because the bubbling flow rate is higher and more mass is made available, aerosol generation increases with higher vibration intensities. This effect was clearly visible during the fluidizer performance tests described in Section 3.1, when stepwise increasing of either frequency or amplitude resulted in a respective increase of the particle number concentration. Particle release at the surface of the bubbling bed happened via the airflow above the powder bed surface. Higher flow rates generate stronger drag so that larger (i.e. heavier) particles can be moved against gravity. Consequently, more particles are released. In the fluidizer performance tests, when increasing the flow rate while continuously shaking, aerosol generation also increased. Above a flow rate of 0.3 slm, the particle number concentration did not increase further. We therefore presume that the sample flow rate that we used during the dustiness tests was sufficient to pick up all liberated individual fibres and agglomerates that were ejected alongside the much larger powder particles.

Higher vibration intensities also led to de-agglomeration being more effective and leading to more particles being liberated. We considered that the liberation of surface fibres was the dominant de-agglomerating mechanism. We assumed that the number of entangled fibres and so the binding strength between agglomerates increased with agglomerate size, requiring more energy to overcome. Consequently, the average particle size in the aerosol should be larger at higher vibration intensities. Agglomerate sizes within aerosol samples were determined from the measured projection areas of agglomerates using SEM. For NTX-3, the material with the largest spheroidal agglomerate fraction (ca. 40%), the count median diameter of the agglomerate size distribution increased from ca. 250 nm at  $\Gamma = 1.8$  to ca. 800 nm at  $\Gamma = 5$ . For the other materials, the number of agglomerates was insufficient to justify a fit to the size distribution. However, mean diameters showed an increasing trend. Taking Baytubes C150P as an example, the material with the largest agglomerates, mean agglomerate sizes increased from ca. 1500 nm at  $\Gamma = 1.8$  to 2700 nm at  $\Gamma = 5$ . Note that for Baytubes C150P, aerosol agglomerates exhibited diameters similar to the smallest agglomerates being adherent to the surfaces of powder particles which corroborates our assumption, that the liberation of surface fibres and agglomerates was the dominant de-agglomeration mechanism in the fluidizer. However, we did not take material samples of the powder immediately after the dustiness tests and analysed them with the SEM to corroborate our interpretation. According to our analysis, powder particles of Baytubes C150P should show smoother surfaces after the dustiness test. Such a study could further analyse the de-agglomerating nature of the vibro-fluidized bed.

To summarize, during most dustiness tests, a bubbling fluidized bed was gradually formed by breaking entanglements between powder particles until a steady state was reached. In that period, the minimum fluidization velocity decreased while the bubbling flow rate and bubble size rose. Consequently, the amount of material transported upwards increased. In parallel, de-agglomeration of powder particles created a

constant supply of individual fibres and agglomerates in the powder. When the bubble wake was ejected upon the emerging to the bed surface, individual fibres and agglomerates could be picked up by the airstream. As a consequence, the generated particle number concentration first increased, eventually stabilized and kept stable over the course of the dustiness tests.

Baytubes C150P and MRCS D showed decreasing particle number concentration at the higher vibration intensity after the initial peak. For Baytubes C150P, this might have been due to a lower number of surface fibres and agglomerates compared to other materials. In the time of the dustiness test, their reservoir in the powder bed depleted quickly. To test this theory, additional tests are necessary, with much longer durations of aerosol generation. Other materials with a greater reservoir of fibres and agglomerates that can be liberated might show a much slower decrease of particle number concentration, not visible in the time of the dustiness tests used in this study. The nature of the MRCS D-powder and dust calls for a different explanation. The powder of MRCS D comprised many impurity particles such as carbon fibres that might break easily with vibrational agitation. This led to an immediate release of non-fibrous carbon fibre fragments besides MWCNTs. Accordingly, different to the other materials, the impurity fraction for MRCS D was much higher at  $\Gamma = 5$ .

The particle number concentration of MWCNT-7 and NM401, as shown for MWCNT-7 in Fig. 6 (b), dropped back to background level following an initial peak upon start of the shaker unit and sample flow rate. For both materials, fluidization was not observed under any conditions of aerosol generation. Vibrational agitation was ineffective because of the low weight of the powder particles (small size and low density), resulting in lesser kinetic energy of the individual powder particles, not sufficient to break them apart. In parallel, powder particle exhibited many interlocked surface fibres. The combination of low strain on particles with strong cohesiveness caused the powder bed to remain packed. Accordingly, the airflow most likely bypassed through channels forming long void areas in the powder bed. We therefore assume that initially particles weakly bound to the powder bed were aerosolized by the channel airflow. Their reservoir depleted over time, resulting in decreasing particle number concentration. At  $\Gamma = 5$ , for one of three runs of dustiness tests, the concentration peaks again late in the dustiness test. It might be possible that the constant agitation of the powder caused a build-up of strain in the powder bed that at one point caused channels to collapse and reform elsewhere in the powder bed. Consequently, the process of aerosol generation repeated itself.

The reasons for the formation of mm-sized particles bouncing on the powder bed of MWCNT-7 and NM401 remains speculative. It might be possible that particles on the surface of the powder could move more freely, harvesting other particles in the process. Over time, particles would agglomerate to large mm-sized clods that bounced on the vibrating powder surface. Here, the fluidizer would have had the opposite effect, not breaking interlocking of particles but further entangling and agglutinating powder material.

#### 4.2. Aerosol stability

The particle number concentration of fluidized beds were seemingly stable over a long period of time, indicating stable aerosol generation. We used the statistical variance coefficient  $\nu$  of measurands for a group of data points of the particle number concentration time series, i.e. the ratio of standard deviation and arithmetic mean. Fig. 7 shows the average variance coefficients of the data range representing 60 min of continuous measurement, 15 min after starting the aerosol generation with the fluidizer. For the materials with fluidized beds, the variance coefficients were  $0.08 < \nu < 0.26$  and  $0.05 < \nu < 0.15$  for  $\Gamma = 1.8$  and  $\Gamma = 5$ , respectively. Continuous fluidization of a powder bed accompanied by stable particle number concentration would allow deriving time-independent measurands, such as the average particle number concentration.

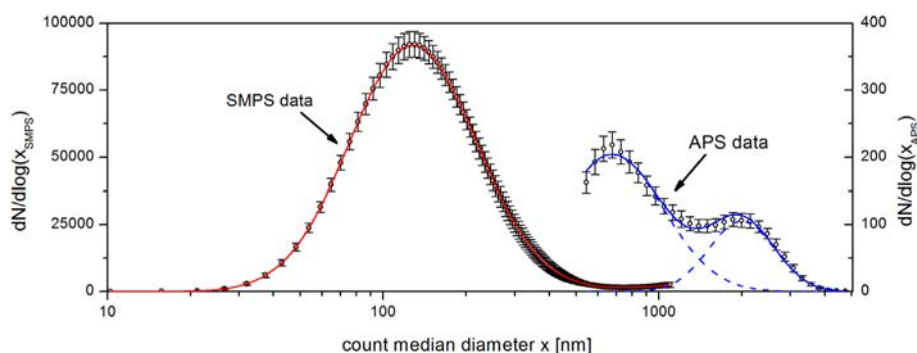


Fig. 7. Average particle size distributions measured with the SMPS and APS during a dustiness test with C2154 at vibration intensity  $\Gamma = 1.8$ .

The mono-modal size number distributions that were observed with the SMPS showed low variability over the course of a fluidizer experiment according to the experimental uncertainty of the count-median diameter and geometric standard deviation. It is thereby reasonable to assume that the quality of the aerosol, i.e. the sizes of morphological fractions, did not change. Variance coefficients were in the range of 0.02–0.15 and 0.01–0.14 for the count-median diameter and geometric standard deviation, respectively. When interpreting our data, one must keep in mind that the SMPS has many limitations for both size classification and counting of fibres. The bipolar charging when applied to fibre aerosols might not result in a Boltzmann charge distribution as is assumed by the SMPS data evaluation algorithm [51,52]. The DMA transfer functions for fibres of different lengths and diameters are currently uncharacterized, so size classification based on electrical mobility diameter is impossible to interpret. However, electrical mobility of MWCNTs seem to scale more with length than diameter [53]. Our data corroborates this observation, since the mode values of the lognormal fits of the size distribution measured for the aerosols show a trend towards larger median nanotube length for materials (Table 3). In addition, MWCNT material deposited inside of the DMA may get charged so that they experience a repulsive force, ultimately resulting in nanotubes bouncing between the electrodes. These particle motions may disturb aerosol and sheath flows, leading to a mixing of unclassified with classified fibres that both exit the monodisperse outlet of the DMA [54]. Thereby, particle counts in a certain size channel might be overestimated and thus quantitative measurement results of the SMPS for MWCNTs seem non-plausible.

The APS is used to measure the size distribution of larger particles on the basis of the aerodynamic diameter, which depends on the particle's inertia and flow cross-section in a laminar flow. In this regime, elongated objects like fibres are aligned so that their flow cross-section is minimal [55]. CNTs therefore appear to have higher aerodynamic diameters compared to spheroidal particles with equivalent inertia. Agglomerates with more spherical shapes do not show a large alignment effect. We assume the first peak to be comprised of individual fibres and fibrous agglomerates, shifted accordingly to larger diameters in comparison to their electrical mobility diameter. The second peak consisted of large agglomerates. Compared to the CPC and SMPS, the APS concentrations were usually much lower. This might be partly because the first peak does not appear in the size distribution. We also speculate that the APS has a low counting efficiency towards MWCNTs. However, to the authors' knowledge, no systematic studies on counting efficiencies of aerosol instruments for fibre aerosols have been conducted. Similar APS aerodynamic size distributions for MWCNT aerosols released by both a nebulizer and a two-component fluidized bed were observed [56].

#### 4.3. Ranking of materials

Ranking based on one property measured for a representative ensemble of subjects allows the definition of property bands. With aerosol

monitoring alone, we could rank the materials based on their average particle number concentrations. With the help of the morphological characterization, we were able to differentiate between the average number concentrations of individual fibres and WHO-fibres. For risk related properties, e.g. the dustiness of WHO-fibres, such banding can be used in risk grouping strategies [8].

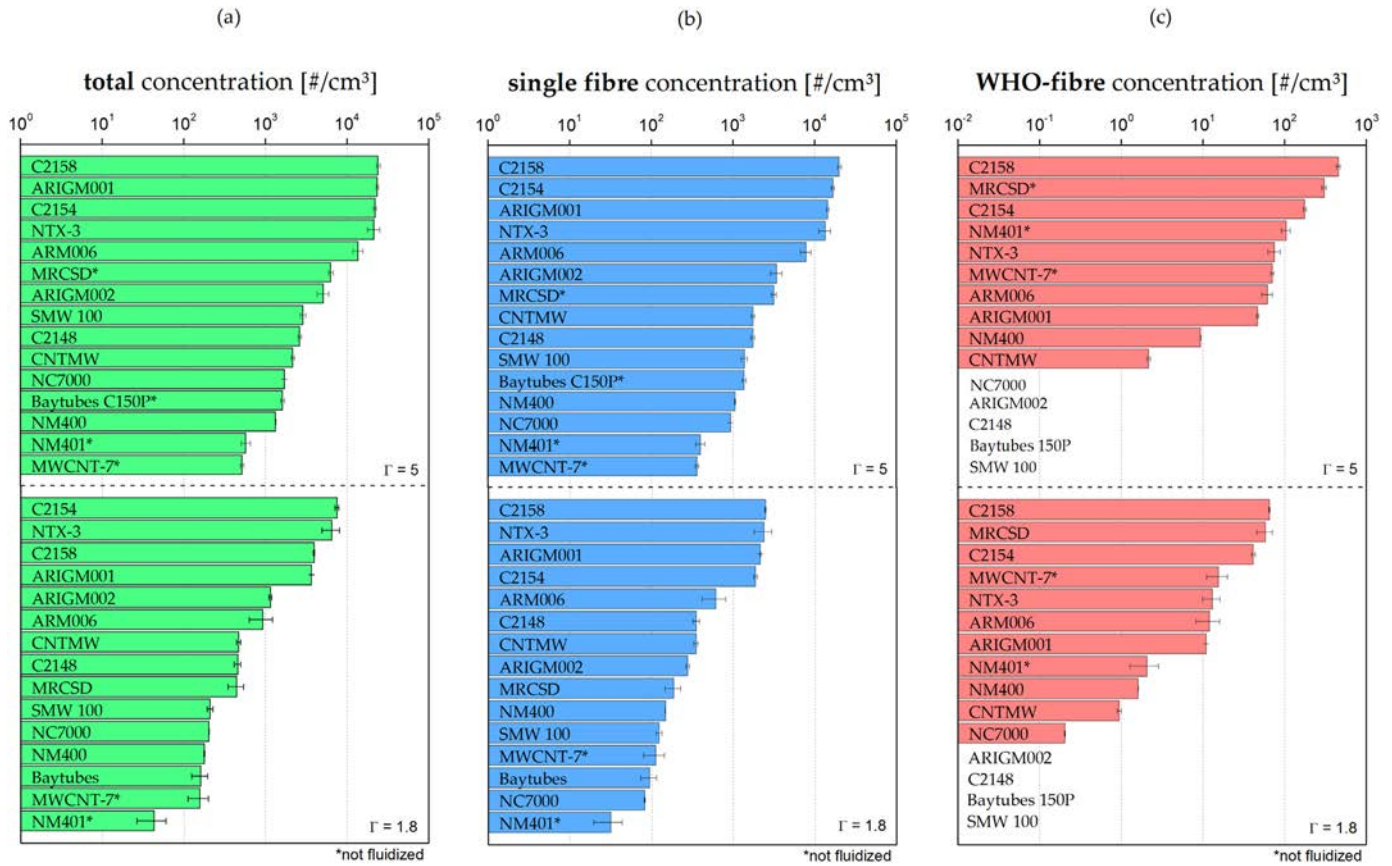
Fig. 8 (a) shows the ranked results for the average particle number concentrations without morphology fractionation, i.e. the total number concentration. Remember that the materials NM401 and MWNT-7 were not fluidized during the dustiness test. For  $\Gamma = 5$ , the materials MRCS and Baytubes C150P were likewise not fluidized. The material ranking for all tested MWCNTs did not depend significantly on vibration intensity, except for ARM006, which showed dustiness at  $\Gamma = 5$  to be one order of magnitude higher than at  $\Gamma = 1.8$ .

Fig. 8(b) shows the average individual fibre number concentration measured with CPC assuming an individual fibre fraction equivalent to the percentages in Table 4. No major changes in ranking occurred compared to the ranking by averaged particle number concentrations.

Fig. 8(c) shows the ranking of concentrations of WHO-fibres. Even though the fraction of WHO fibres for C2158 was only around 2%, its high dustiness led to the highest release of WHO-fibres of all materials. In contrast, the materials NM401 and MWNT-7 had a relatively high fraction of WHO-fibres, but a much smaller dustiness leading to a much lower concentration of WHO-fibres. The material MRCS had a moderate dustiness but due to the relatively large fraction of WHO-fibres showed one of the highest concentrations of WHO-fibres. The materials ARIGM002 and C2148, which were materials of moderate dustiness, did not release hardly any WHO-fibres. This analysis shows that dustiness tests, without proper morphological characterization, cannot assess the propensity of a powder to release WHO-fibres.

To the authors knowledge, such a material ranking for CNTs was shown only once [24]. The ranking was built on number- and mass-based dustiness indexes determined with the vortex shaker dustiness test. Of the 14 MWCNT materials tested in that study, two of them, namely NM400 and NM401, were tested here as well. As discussed earlier, dustiness indices determined from online monitoring instruments during the fluidizer test were stable, contrary to the vortex shaker test. Therefore, a quantitative comparison of the obtained indexes of both studies is not justified.

According to the fibre toxicological paradigm, biopersistent fibres of WHO geometry are considered more toxic when respired than granular particles or fibres shorter than 5  $\mu\text{m}$ . Therefore, a material ranking based on average number concentration of WHO-fibres can be directly related to inhalative exposure-related risks. In most European countries, occupational exposure levels (OEL) for WHO fibres are in the range from 40 to 10,000 WHO-fibres per  $\text{m}^3$  (0.004 to 0.1 WHO-fibres per  $\text{cm}^3$ ). Considering a scenario in which particles are released from a powder at low energy input as represented by the fluidizer, even after mixing with ambient air free of fibres, WHO-fibres of the materials ARIGM001, ARM006, C2154, C2158, MRCS, MWNT-7 and NTX-3



**Fig. 8.** Average particle number concentrations measured over the course of the dustiness test at vibration intensities 1.8 (bottom graphs) and 5 (top graphs). Results are displayed on a logarithmic scale and ranked. Here, (a) depicts the total concentrations, i.e. results obtained with the CPC without morphology fractionation, (b) the concentrations of individual fibres obtained after morphological classification and (c) the concentration of objects matching the WHO criteria for critical fibres (length > 5  $\mu\text{m}$ , diameter < 3  $\mu\text{m}$ , aspect ratio > 3:1), comprising individual fibres and agglomerates with fibrous shape, obtained after morphological classification and measurement of their length and diameter.

have a high emission propensity and may exceed OELs if handled carelessly.

#### 4.4. Recommendations for an optimized fluidizer dustiness test

Based on the discussion of the dustiness tests with MWCNTs we can outline recommendations for optimized dustiness testing procedure using the fluidizer.

- Dustiness tests are typically designed in accordance with specific powder handling procedures. For future development of the fluidizer towards a dustiness test standard, its representativity for one or several selected classes of powder processing steps should be clarified. The fluidizer presented here allows stable aerosol generation over a long period of time, which is beneficial for aerosol generation applications. Possible relevant scenarios our fluidizer may mimic successfully are handlings or procedures that continuously process powders. Typical applications may base on wind sifting of powders for, e.g., drying and coating purposes [57,58]. Vibro-fluidized beds are also used for multiphase chemical reactions with the powder grains acting as catalyst particles [59].
- Many handlings are short-term actions. An alternative application of the fluidizer method may comprise shaking with well-controlled operation conditions lasting only for a short period of time, e.g. a few seconds, to represent such short-term actions. The resulting emission concentration spike is monitored and dustiness indexes are determined for the emission spike. Such a test design would be more appropriate for the study of short-term dust emissions. However, aerosol sampling would result in very low deposition densities, considering the relatively low volume sampled. Consequently, the routine

to determine morphological information would require a large filter area to be analysed with SEM to obtain relevant particle statistics.

- For a more disentangled state of the powder beds, it might be advisable to perform a period of shaking before switching on the sample flow rate. Establishment of stationary fluidized beds might be facilitated.
- The fluidizer dustiness test should be performed for fluidized powder beds only. To allow monitoring the expansion of the powder bed continuously, the main metal tube of the test setup sample should be replaced with a transparent tube with inside conductive coating.
- We stored the powders in a desiccator for near 0% relative humidity. Dustiness testing according to preEN 17199 considers using a relative humidity of 50% during storage. Powders to be tested with the fluidizer should be stored in e.g. a climate chamber for temperature and humidity control of the atmosphere.
- Similarly, preEN 17199 prescribes a relative humidity of 50% of the test atmosphere as well. For dustiness testing with the fluidizer, humidity control should be incorporated into the experimental setup.
- Data evaluation should start when the particle number concentration has stabilized to derive time-independent dustiness measurands.
- Sampling for morphological analysis should also start after stabilization of the particle number concentration to be able to extrapolate the average particle number concentration during collection time. This way, dustiness measurands could be determined with two complementary methods.
- A fluidizer frequency of  $f = 30$  Hz and an amplitude of  $A = 0.5$  mm resulting in a vibration intensity of  $\Gamma = 1.8$  was found to fluidize the majority of studied MWCNTs. For other types of materials, other parameters may be suited better. As mentioned above, for MWCNT vibration intensity had no significant influence on the material

ranking. For other materials, this might not be the case. Fibres more fragile than CNTs like cup-stacked carbon nanofibres could break during shaking with higher energy input, adding an additional aspect to powder fragmentation apart from deagglomeration.

- As long as the response of the SMPS to polarizable high aspect-ratio particles is not fully understood, data obtained with the instrument add no value to a dustiness test. Similarly, since the APS cannot detect individual fibres, only the agglomerated fraction might be determined. Total concentrations measured with the two instruments can therefore not be interpreted with respect to emitted fibre concentrations. Accordingly, out of the instruments used in this study, we can recommend only using a CPC, since its measurement principle is independent from particle shape.
- The morphological characterization by means of SEM analysis of track-etched membrane filter samples is an indispensable requirement to determine the health-relevant fraction of WHO-fibres. The authors are convinced that size of the WHO-fibre fraction and, alternatively, the average concentration of WHO-fibres are the most important measurands.
- The main sources for errors in the morphological characterization of the samples are (1) Subjective interpretation of counting rules, which led to deviations of the sizes of the morphology fractions between persons and (2) a too small number of evaluated particles. One should make sure beforehand to count enough particles for a relative error of 5% at a confidence level of 95%.

## 5. Summary and conclusions

Aerosols were generated from the powder beds of various MWCNT materials using the fluidizer. Individual fibres and small agglomerate fragments stemming from de-agglomeration of powder particles were emitted. The individual fibre fraction showed the largest cardinality in the morphology class distribution. The aerosol generation mechanism is a mixture of bubbling fluidization and bed vibration that can be adapted with high flexibility to the testing requirements.

Depending on the energy input, determined by the vibration intensity, different states of the powder bed could be established. An optimal energy input of  $\Gamma = 1.8$  was found to fluidize all tested MWCNT materials, except two. Stable bubbling rates resulted in stable particle number concentrations. Under our testing conditions, measured average particle number concentrations varied by about three orders of magnitude for the studied materials.

A ranking of materials according to their total dust release propensity was possible utilizing the average particle number concentration. Comprehensive morphological characterization was performed by analysing track-etched membrane filter samples by means of electron microscopy. This allowed risk-related ranking of MWCNT powders by their propensity to emit individual fibres and fibres or fibre shaped agglomerates matching the WHO-fibre criteria. Particularly for the number of WHO-fibres emitted, the ranking differed strongly from the ranking of overall dustiness. For example ARIGM002, showing one high dustiness based on aerosol monitoring, did not emit any WHO-fibres, whereas C2154 and C2158 ranked both high in overall dustiness and WHO-fibre emission and MRCSO only moderate for overall dustiness but high for WHO-fibres. Thus to determine the hazardous potential of MWCNT powders the monitoring with online measurement devices is not sufficient, but filter samples and a morphological analysis by an imaging method is required.

Comparing the measurements at  $\Gamma = 1.8$  and  $\Gamma = 5$  did not result in major changes of ranking in overall dustiness, numbers of individual fibres emitted or WHO-fibres emitted, provided that a fluidized bed was established. The measurement of number concentrations with the SMPS is prone to errors and no valuable information could be gained from average particle size distributions. The APS data were either already

covered by the CPC, or were several orders of magnitude lower than the CPC data. Therefore, the measurement of number concentrations with the CPC alone and at  $\Gamma = 1.8$  appears sufficient.

The aim of this study was to introduce the fluidizer, an aerosol generator achieving disentanglement of agglomerates in individual fibres, resulting in a large fibre fraction. In addition, with the help of counting rules for a morphological characterization of aerosol samples collected during aerosol generation, we aimed to perform dustiness tests for MWCNT-powders that were able to determine the WHO-fibre fraction of the aerosol, to measure the most health-relevant fibre dustiness measurand, namely WHO-fibre concentration.

## 6. Outlook

In future work, other high aspect ratio materials like single-walled CNTs and nanofibres of different materials will be tested with the fluidizer method presented here. This promises to allow for further differentiation or generalization of the conclusions drawn here on the relevance and applicability of the technique.

We speculated on different mechanisms for de-agglomeration, which are ultimately responsible for continuous aerosol generation. At different energy inputs, one or more mechanisms might occur or dominate de-agglomeration. Aerosol samples taken for different temporal behaviours of the particle number concentration accompanied with characteristic fluidized bed behaviours might provide more insight into the de-agglomerating mechanisms of the fluidizer.

The fluidizer setup could also be applied to generate exposure atmospheres for in vivo or in vitro fibre toxicological inhalation studies. Stable and continuous particle number concentration provides a good control over the exposure dose depending on exposure duration. Furthermore, to study the fibre toxicological paradigm for nanofibres like nanotubes, the fluidizer provides a high individual fibre fraction in the exposure atmosphere, which is of high importance for such studies [60].

## Acknowledgements

The authors would like to thank Judith Neuhoff, Simon Schröder, Mikolaj Jandy, Doris Perseke, Jana Thiel and Dominic Kehren who contributed greatly to this work during method development or data gathering in form of the morphological characterization as well as improving this manuscript.

This work was supported by the European Union Seventh Framework Programme (FP7/2007-2013) [grant agreement No. 310584 (NANOREG)]; and the German Federal Ministry of Education and Research [grant agreement No. FKZ 03XP0002B, nanoGRAVUR].

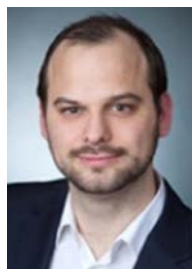
## Appendix A. Supplementary data

Supplementary data to this article can be found online at <https://doi.org/10.1016/j.powtec.2018.10.013>.

## References

- [1] P.J.F. Harris, *Carbon Nanotube Science: Synthesis, Properties and Applications*, Cambridge University Press, Cambridge, 2009.
- [2] K. Donaldson, R. Aitken, L. Tran, V. Stone, R. Duffin, G. Forrest, A. Alexander, Carbon nanotubes: a review of their properties in relation to pulmonary toxicology and workplace safety, *Toxicol. Sci.* 92 (2006) 5–22.
- [3] K. Donaldson, C. Poland, New insights into nanotubes, *Nat. Nanotechnol.* 4 (2009) 708–710.
- [4] C. Poland, R. Duffin, K. Donaldson, in: S. Sahu, D. Casciano (Eds.), *Nanotoxicity- From In Vivo and In Vitro Models to Health Risks*, John Wiley & Sons, 2009.
- [5] S. Rittinghausen, A. Hackbarth, O. Creutzenberg, H. Ernst, U. Heinrich, A. Leonhardt, D. Schaudien, The carcinogenic effect of various multi-walled carbon nanotubes (MWCNTs) after intraperitoneal injection in rats, *Part. Fibre Toxicol.* 11 (2014) 18.
- [6] P. Jackson, K. Kling, K.A. Jensen, P.A. Clausen, A.M. Madsen, H. Wallin, U. Vogel, Characterization of genotoxic response to 15 multiwalled carbon nanotubes with variable physicochemical properties including surface functionalizations in the FE1-Muta(TM) mouse lung epithelial cell line, *Environ. Mol. Mutagen.* 56 (2015) 183–203.

- [7] T. Kasai, Y. Umeda, M. Ohnishi, T. Mine, H. Kondo, T. Takeuchi, M. Matsumoto, S. Fukushima, Lung carcinogenicity of inhaled multi-walled carbon nanotube in rats, *Part. Fibre Toxicol.* 13 (2016) 53.
- [8] T.A.J. Kuhlbusch, S.W.P. Wijnhoven, A. Haase, Nanomaterial exposures for worker, consumer and the general public, *NanoImpact* 10 (2018) 11–25.
- [9] K.H. Dunn, A.C. Eastlake, M. Story, E.D. Kuempel, Control banding tools for engineered nanoparticles: what the practitioner needs to know, *Ann. Work Expos. Health* 62 (2018) 362–388.
- [10] D.E. Evans, L.A. Turkevich, C.T. Roettgers, G.J. Deye, P.A. Baron, Dustiness of Fine and Nanoscale Powders, *Ann. Occup. Hyg.* 57 (2013) 261–277.
- [11] Y. Ding, B. Stahlmecke, A.S. Jiménez, I.L. Tuinman, H. Kaminski, T.A.J. Kuhlbusch, M. van Tongeren, M. Riediker, Dustiness and deagglomeration testing: interlaboratory comparison of systems for nanoparticle powders, *Aerosol Sci. Technol.* 49 (2015) 1222–1231.
- [12] EN 15015, Workplace Exposure - Measurement of the Dustiness of Bulk Materials, 2013.
- [13] prEN 17199, Workplace Exposure - Measurement of Dustiness of Bulk Materials that Contain or Release Nano-Objects or Submicrometer Particles, 2017.
- [14] T. Gebel, H. Foth, G. Damm, A. Freyberger, P.-J. Kramer, W. Lilienblum, C. Röhl, T. Schupp, C. Weiss, K.-M. Wollin, J. Hengstler, Manufactured nanomaterials: categorization and approaches to hazard assessment, *Arch. Toxicol.* (2014) 1–21.
- [15] R. Mihalache, J. Verbeek, H. Graczyk, V. Murashov, P. van Broekhuizen, Occupational exposure limits for manufactured nanomaterials, a systematic review, *Nanotoxicology* 11 (2017) 7–19.
- [16] World Health Organization, Determination of Airborne Fibre Number Concentrations: A Recommended Method, by Phase-Contrast Optical Microscopy (Membrane Filter Method) 1997.
- [17] D. Dahmann, C. Monz, Determination of dustiness of nanostructured materials, *Gefahrstoffe - Reinhaltung Luft* 71 (11–12) (2011) 481–487.
- [18] T. Schneider, K.A. Jensen, Combined single-drop and rotating drum dustiness test of fine to nanosize powders using a small drum, *Ann. Occup. Hyg.* 52 (2008) 23–34.
- [19] M. Morgener, O. Le Bihan, A. Ustache, O. Aguerre-Chariol, Experimental study of the aerosolization of fine alumina particles from bulk by a vortex shaker, *Powder Technol.* 246 (2013) 583–589.
- [20] O. Isamu, S. Hiromu, G. Masashi, Dustiness testing of engineered nanomaterials, *J. Phys. Conf. Ser.* 170 (2009), 012003.
- [21] B.K. Ku, G. Deye, L.A. Turkevich, Characterization of a vortex shaking method for aerosolizing fibers, *Aerosol Sci. Technol.* 47 (2013) 1293–1301.
- [22] O. Isamu, H. S. G. Masashi, Dustiness testing of engineered nanomaterials, *J. Phys. Conf. Ser.* 170 (2009) 1293–1301.
- [23] O.L.C. Le Bihan, A. Ustache, Lien, D. Bernard, O. Aguerre-Chariol, M. Morgener, Experimental study of the aerosolization from a carbon nanotube bulk by a vortex shaker, *J. Nanomater.* 2014 (2014) 11.
- [24] C. Dazon, O. Witschger, S. Bau, R. Payet, K. Beugnon, G. Petit, T. Garin, L. Martinon, Dustiness of 14 carbon nanotubes using the vortex shaker method, *J. Phys. Conf. Ser.* 838 (2017), 012005.
- [25] S.C. Kim, D.R. Chen, C. Qi, R.M. Gelein, J.N. Finkelstein, A. Elder, K. Bentley, G. Oberdorster, D.Y. Pui, A nanoparticle dispersion method for in vitro and in vivo nanotoxicity study, *Nanotoxicology* 4 (2010) 42–51.
- [26] B. Simonow, A. Meyer-Plath, D. Wenzlaff, S. Plitzko, Dry aerosolization technique for continuous and stable generation of carbon nanotube aerosols containing a large fraction of individual fibres, *NanoSafe 2016* Grenoble, France, 2016.
- [27] K.R. Spurny, C. Boose, D. Hochrainer, Zur Zerstäubung von Asbestfasern in einem Fließbett-Aerosolgenerator, *Staub, Reinhaltung Luft* 35 (1975) 440–445.
- [28] K.R. Spurny, Preparation of size-selected fibers and fibrous aerosols for biological experiments, *Environ. Int.* 4 (1980) 39–46.
- [29] S.G. Plitzko, Erhardt; Dziurawitz, Nico; Broßell, Dirk, Erzeugung von CNT/CNF-Stäuben mit einem Schwingbett-Aerosolgenerator und Charakterisierung der Fasermorphologie mithilfe eines Thermalpräzipitators als Sammelsystem, *Gefahrstoffe - Reinhaltung Luft* 1-2 (2010) 31–35.
- [30] J.R. van Ommen, J.M. Valverde, R. Pfeffer, Fluidization of nanopowders: a review, *J. Nanopart. Res.* 14 (2012) 1–29.
- [31] J.M. Valverde, A. Castellanos, Fluidization of nanoparticles: a simple equation for estimating the size of agglomerates, *Chem. Eng. J.* 140 (2008) 296–304.
- [32] J.M. Valverde, A. Castellanos, Fluidization, bubbling and jamming of nanoparticle agglomerates, *Chem. Eng. Sci.* 62 (2007) 6947–6956.
- [33] J.M. Valverde, A. Castellanos, Effect of compaction history on the fluidization behavior of fine cohesive powders, *Phys. Rev. E* 73 (2006), 056310.
- [34] C.H. Nam, R. Pfeffer, R.N. Dave, S. Sundaresan, Aerated Vibrofluidization of Silica Nanoparticles, *AIChE J.* 50 (2004) 1776–1785.
- [35] S.J. Moon, I.G. Kevrekidis, S. Sundaresan, Particle simulation of Vibrated Gas-Fluidized Beds of Cohesive Fine Powders, *Ind. Eng. Chem. Res.* 45 (2006) 6966–6977.
- [36] D. Geldart, Types of gas fluidization, *Powder Technol.* 7 (1973) 285–292.
- [37] C.M. White, R. Banks, I. Hamerton, J.F. Watts, Characterisation of commercially CVD grown multi-walled carbon nanotubes for paint applications, *Prog. Org. Coat.* 90 (2016) 44–53.
- [38] I. Alig, P. Pötschke, D. Lellinger, T. Skipa, S. Pegel, G.R. Kasaliwal, T. Villmow, Establishment, morphology and properties of carbon nanotube networks in polymer melts, *Polymer* 53 (2012) 4–28.
- [39] J.R.V. Ommen, R. Pfeffer, Fluidization of Nanopowders: Experiments, Modeling, and Applications, *Engineering Conferences International, ECI Digital Archives* 2010.
- [40] J. Visser, Van der Waals and other cohesive forces affecting powder fluidization, *Powder Technol.* 58 (1989) 1–10.
- [41] D. Harrison, L.S. Leung, Bubble formation at an orifice in a fluidized bed, *Nature* 190 (1961) 433.
- [42] C. Dechsiri, Particle Transport in Fluidized Beds, University Medical Center Groningen, University of Groningen, 2004.
- [43] M. Rhodes, What is turbulent fluidization? *Powder Technol.* 88 (1996) 3–14.
- [44] S. Kaliyaperumal, S. Barghi, L. Briens, S. Rohani, J. Zhu, Fluidization of nano and sub-micron powders using mechanical vibration, *Particuology* 9 (2011) 279–287.
- [45] C. Zhu, G.L. Liu, Q. Yu, R. Pfeffer, R.N. Dave, C.H. Nam, Sound assisted fluidization of nanoparticle agglomerates, *Powder Technol.* 141 (2004) 119–123.
- [46] Y.Y. Huang, E.M. Terentjev, Dispersion of carbon nanotubes: mixing, sonication, stabilization, and composite properties, *Polymer* 4 (2012) 275.
- [47] T. Novák-Szabó, A.Á. Sáros, S. Shaw, D. Bertoni, A. Pozzebon, E. Grotto, G. Sarti, P. Ciavola, G. Domokos, D.J. Jerolmack, Universal characteristics of particle shape evolution by bed-load chipping, *Sci. Adv.* 4 (2018).
- [48] C. Asbach, A. Meyer-Plath, S. Clavaguera, M. Fierz, L. MacCalman, C. Alexander, A.M. Todea, I. Iavicoli, Assessment of Personal Exposure to Airborne Nanomaterials - a Guidance Document, 2016.
- [49] W. Hinds, Aerosol Technology-Properties, Behavior, and Measurement of Airborne Particles, Second Edition John Wiley and Sons, 1999.
- [50] I. 13322-1, Particle size analysis - Image analysis methods-Part1: static image analysis methods, 2004.
- [51] Y. Kunitoshi, A. Seiji, N. Yoshikazu, Orientation and purification of carbon nanotubes using ac electrophoresis, *J. Phys. D. Appl. Phys.* 31 (1998) L34.
- [52] B.T. Chen, D. Schwegler-Berry, A. Cumpston, J. Cumpston, S. Friend, S. Stone, M. Keane, Performance of a scanning mobility particle sizer in measuring diverse types of airborne nanoparticles: multi-walled carbon nanotubes, welding fumes, and titanium dioxide spray, *J. Occup. Environ. Hyg.* 13 (2016) 501–518.
- [53] P. Baron, G. Deye, J. Fernback, Length separation of fibers, *Aerosol Sci. Technol.* 21 (1994) 179–192.
- [54] B.K. Ku, A.D. Maynard, P.A. Baron, G.J. Deye, Observation and measurement of anomalous responses in a differential mobility analyzer caused by ultrafine fibrous carbon aerosols, *J. Electrostat.* 65 (2007) 542–548.
- [55] J.-Z. Lin, J. Li, W.-F. Zhang, Orientation distribution of fibres in a channel flow of fibre suspension, *Chin. Phys.* 14 (2005) 2529.
- [56] S.-B. Lee, J.-H. Lee, G.-N. Bae, Size response of an SMPS-APS system to commercial multi-walled carbon nanotubes, *J. Nanopart. Res.* 12 (2010) 501–512.
- [57] S. Soponronnarit, S. Wetachama, S. Trutassanawin, W. Jariyontontvatt, Design, testing, and optimization of vibro-fluidized bed paddy dryer, *Dry. Technol.* 19 (2001) 1891–1908.
- [58] D.E. Wurster, Air-suspension technique of coating drug particles - a preliminary report, *J. Am. Pharm. Assoc.* 48 (1959) 451–454.
- [59] H. Masuda, K. Higashitani, H. Yoshida, *Powder Technology Handbook - Third Edition*, Taylor & Friends Group, 2006.
- [60] W.W. Polk, M. Sharma, C.M. Sayes, J.A. Hotchkiss, A.J. Clippinger, Aerosol generation and characterization of multi-walled carbon nanotubes exposed to cells cultured at the air-liquid interface, *Part. Fibre Toxicol.* 13 (2016).



**Dirk Broßell** has worked as a scientist at the Federal Institute for Occupational Safety and Health since 2009. As a physicist, he received his PhD from Delft University of Technology in 2016. For his doctoral thesis, he developed instruments for nanoparticle characterization. Since then, he has been researching ideas to assess the risk of nanotubes based on material properties and dustiness testing.



**Elisabeth Heunisch** graduated in Molecular Science in 2009. She then worked for the Helmholtz-Centre Berlin as a scientist, doing research in the field of quantum dots for photovoltaics, receiving her PhD at the Free University Berlin in 2013. Since 2015, she is a scientist at the Federal Institute for Occupational Safety and Health, assessing the risk of high aspect ratio materials based on morphology and dustiness.



**Asmus Meyer-Plath** works as senior scientist at BAuA, the Federal Institute for Occupational Safety and Health in Berlin, Germany. Trained as physicist, he received his PhD in plasma chemistry at the University of Greifswald and transmuted to a materials science expert on the synthesis, functionalization and characterization of nanomaterials. He is now active in the field of exposure and risk assessment of nanoparticles and has a strong focus on micro- and nanoscale fibres.



**Daphne Bäger** completed her Master's degree in process engineering and has been working at the Federal Institute for Occupational Safety and Health since 2016. She deals with the morphology of fibrous (nano)materials and their release in the context of workplace measurements.



**Carmen Thim** is a chemical technician and works for the Federal Institute for Occupational Safety and Health since 1993. She performs SEM-analyses of aerosol samples from dustiness tests and workplace samplings as well as develops software tools for SEM-control.



**Volker Bachmann** holds a position as scientist at the Federal Institute for Occupational Safety and Health (BAuA) in Berlin since 2010. His focus is on standardization processes in exposure assessment and on nanomaterial and advanced material related regulation, i.e. REACH. A chemical engineer by training he received his PhD from the University of Utrecht (NL) on synthesis and characterization of luminescent material.



**Daniela Wenzlaff** joined the Federal Institute for Occupational Safety and Health in 2008 and performs as well as evaluates dustiness tests.



**Kerstin Kämpf** graduated in nanostructure sciences and earned her PhD at Technical University of Darmstadt in the physics department in 2014. After a Postdoc stay in St. Petersburg, Russia, she started working for the Federal Institute for Occupational Safety and Health in 2017. Her research focusses on the standardization of aerosol characterization methods, in particular nanofibres.



**John Schumann** graduated as geodesist and started working for the Federal Institute for Occupational Safety and Health in 2015. He is an expert in software development in the field of surveying, robotics and digital image processing. Currently, he develops a control system of a SEM and the computer-automatic detection of fibrous objects in SEM-images.



**Nico Dziurawitz** graduated environmental process engineering and works for the Federal Institute for Occupational Safety and Health since 2008. His expertise in SEM-analysis, software development for SEM control as well as workplace exposure assessment.



**Sabine Pitzko** joined the Federal Institute for Occupational Safety and Health in 1999 and leads the unit 4.5 "Particulate Hazardous Substance, Advanced Materials" since 2015. She has years of practical experience and broad knowledge in the field of exposure assessment in regard to aerosols, in particular asbestos and vitreous fibres, and has been engaged in risk research in the framework of nanomaterials since 2005.